

Magnetic order in 2D antiferromagnets revealed by spontaneous anisotropic magnetostriction

Maurits J. A. Houmes,^{1,*} Gabriele Baglioni,^{1,*} Makars Šiškins,^{1,*} Martin Lee,¹ Dorye L. Esteras,² Alberto M. Ruiz,² Samuel Mañas-Valero,^{1,2} Carla Boix-Constant,² Jose J. Baldoví,² Eugenio Coronado,² Yaroslav M. Blanter,¹ Peter G. Steeneken,^{1,3} and Herre S. J. van der Zant¹

¹*Kavli Institute of Nanoscience, Delft University of Technology, Lorentzweg 1, 2628 CJ, Delft, The Netherlands*

²*Instituto de Ciencia Molecular (ICMol), Universitat de València, c/Catedrático José Beltrán 2, 46980 Paterna, Spain*

³*Department of Precision and Microsystems Engineering, Delft University of Technology, Mekelweg 2, 2628 CD, Delft, The Netherlands*

The temperature dependent order parameter provides important information on the nature of magnetism. Using traditional methods to study this parameter in two-dimensional (2D) magnets remains difficult, however, particularly for insulating antiferromagnetic (AF) compounds. Here, we show that its temperature dependence in AF MPS₃ (M(II) = Fe, Co, Ni) can be probed via the anisotropy in the resonance frequency of rectangular membranes, mediated by a combination of anisotropic magnetostriction and spontaneous staggered magnetization. Density functional calculations followed by a derived orbital-resolved magnetic exchange analysis confirm and unravel the microscopic origin of this magnetization inducing anisotropic strain. We further show that the temperature and thickness dependent order parameter allows to deduce the material's critical exponents characterising magnetic order. Nanomechanical sensing of magnetic order thus provides a future platform to investigate 2D magnetism down to the single-layer limit.

Layered two-dimensional (2D) magnetic materials offer an emerging platform for fundamental studies of magnetism in the 2D limit. Their stackability into van der Waals heterostructures opens pathways to non-trivial magnetic phases and technological applications, including sensors, memories and spintronic logic devices [1]. In addition to ferromagnetism, first observed in CrI₃ [2] and Cr₂Ge₂Te₆ [3], antiferromagnetism in 2D materials has also been studied in FePS₃ [4] and CrSBr [5]. Antiferromagnetic (AF) materials are of particular technological interest due to their high spin-wave propagation speed and lack of macroscopic stray fields, making them strong candidates for spintronic and magnonic applications [6–10].

For insulating, thin AF materials, such as MPS₃ (M(II) = Fe, Co, Ni), few methods are available to study their intrinsic magnetism. Conventional techniques, such as neutron scattering, magnetization measurement by a superconducting quantum interference device (SQUID) or vibrating sample magnetometry are challenging, due to the small volumes of exfoliated 2D materials. Other methods, suited to 2D materials, require electrical conductance, the presence of specific optical modes or ferromagnetic order; they are therefore difficult to apply [1]. In contrast, strain applied to 2D magnetic materials was shown to be extremely powerful, inducing magnetization reversal [11], reorientating the easy-axis [12], or reversing the exchange interaction [13]. In addition, the direct coupling between strain, resonance frequency and magnetization in membranes of 2D magnets, makes nanomechanical resonance a sensitive method for studying their

phase transitions [14–16]. Here, we show, guided by density functional theory (DFT), that the magnetic order parameter of MPS₃ AF membranes can be quantified through the anisotropy in their magneto-elastic response; from its temperature dependence the critical exponents are determined, and their thickness dependence is investigated.

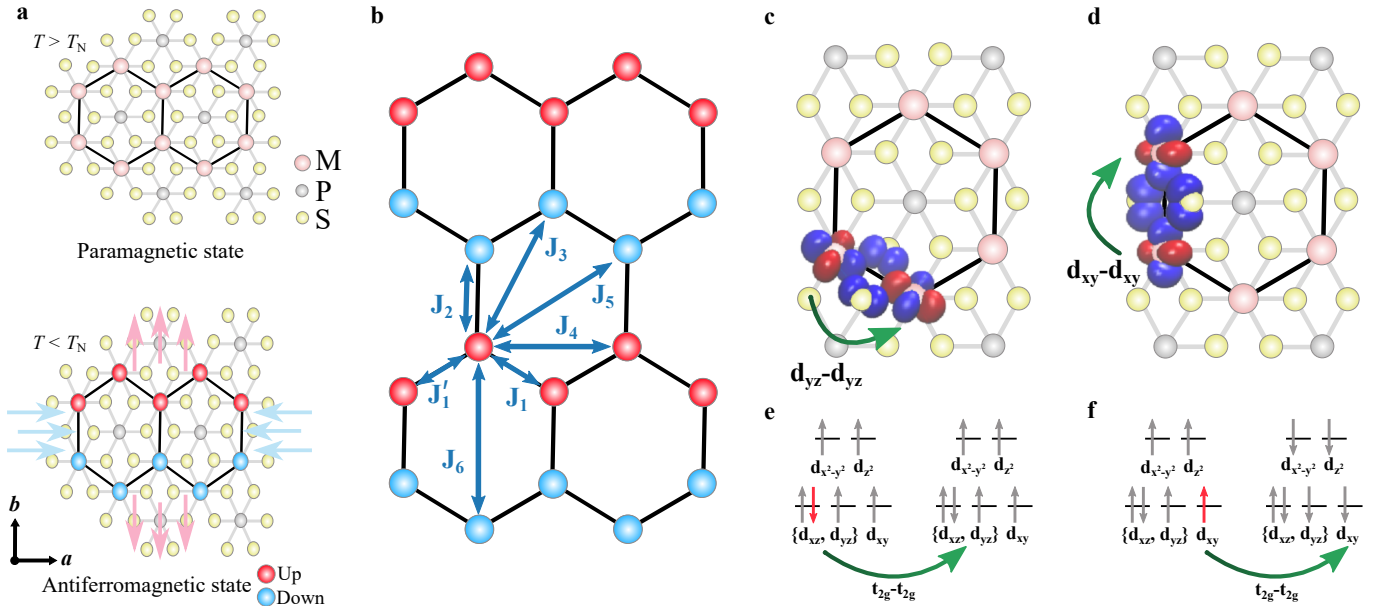
RESULTS AND DISCUSSION

First principles analysis of spontaneous magnetostriction in MPS₃

Transition-metal phosphorus trisulphides, with general formula MPS₃, are layered materials stacked in a monoclinic lattice with symmetry group C2/m [17], as shown in the top view of a single-layer in the paramagnetic phase, Fig. 1a, top panel. The spins of FePS₃ point out-of-plane, whereas both CoPS₃ and NiPS₃ are in-plane systems with their spins preferentially aligned along the *a* axis. The intralayer AF order forms a zigzag configuration, as shown in bottom panel of Fig. 1a, leading to two opposite aligned magnetic sub-lattices. The difference of the magnetisation between these sub-lattices is the Néel vector. In bulk CoPS₃ and NiPS₃, these layers with this staggered magnetism are stacked in a ferromagnetic (FM) fashion with Néel transition temperatures, *T*_N, around 119 and 155 K, respectively [18, 19]. The interlayer magnetic interactions in FePS₃ are AF with a transition around 118 K [20].

To analyse the effect of magnetic ordering on the lattice, we performed first principles structural optimiza-

* These authors contributed equally.



SUPPLEMENTARY FIG. 1. **Magnetostriction in MPS_3 membranes.** **a, top panel,** Crystalline structure of MPS_3 in the paramagnetic phase ($T > T_N$). Black hexagons indicate the organisation of magnetic atoms in the lattice. **a, bottom panel,** Crystalline structure of MPS_3 at the AF phase ($T < T_N$) as it elongates in the b and contracts in the a direction. Light blue and red arrows indicate the axial lattice distortion. **b,** Illustration of the exchange interaction parameters included into the Heisenberg spin Hamiltonian. **c-d,** Calculated maximally localized Wannier orbitals. Green arrows illustrate the most relevant FM superexchange channels for J_1 (J_1') (**c**) and J_2 (**d**), corresponding with the $d_{yz}-d_{yz}$ ($d_{xz}-d_{xz}$) and $d_{xy}-d_{xy}$ orbitals, respectively. **e-f,** Electron configuration of the Fe^{2+} magnetic ions connected by J_1 (**e**) and J_2 (**f**), showing parallel and antiparallel spin orientations, respectively.

tions of $FePS_3$, $CoPS_3$ and $NiPS_3$ based on density functional theory (DFT). For the ground state zigzag magnetic configuration, the calculations predict a compression of the a lattice parameter with respect to the crystallographic, non-magnetic structure of 2.545% and 1.328% for the Co and Fe derivatives respectively (see Table 1). In addition, the b axis expands by 0.402% (Co) and 0.359% (Fe). In contrast, in $NiPS_3$ the lattice parameters remain almost unchanged. The crystal and magnetic structures are strongly connected in these compounds, which is further corroborated by simulations of different spin configurations (see Supplementary Note 1).

The microscopic mechanism governing the spontaneous magnetostriction in these materials is studied using orbital-resolved magnetic exchange analyses based on maximally localized Wannier functions, (see Supplementary Note 1). The analysis shows that the spontaneous magnetostriction calculated in $FePS_3$ and $CoPS_3$ arises from isotropic magnetic exchange interactions between $t_{2g}-t_{2g}$ orbitals. Specifically, for $FePS_3$ the main magnetic exchange channels, substantially affected by the compression of the a and expansion of the b lattice parameters, are the ones involving $t_{2g}-t_{2g}$ interactions of FM nature. The changes in the lattice parameters result in an increase in J_1 and J_1' due to a decrease in distance between the $d_{yz}-d_{yz}$ and $d_{xz}-d_{xz}$ orbitals, respectively (Fig. 1c). Simultaneously, these changes cause a decrease of J_2 due to a larger separation of the $d_{xy}-d_{xy}$ orbitals

(Fig. 1d). This is compatible with the electron configuration of Fe^{2+} (d^6), which has these orbitals partially filled and allows FM hopping between them (Fig. 1e,f).

This hopping effect also occurs for Co^{2+} (d^7) although the additional electron present for Co blocks the $d_{xy}-d_{xy}$ pathway (Supplementary Note 1, Fig. S2). This results in a stronger effect along J_1 and J_1' for the optimized structure, maximizing FM interactions in the zigzag chain, which involve the $d_{yz}-d_{yz}$ and $d_{xz}-d_{xz}$ orbitals, respectively. For the Ni^{2+} derivative (d^8), the t_{2g} energy levels are fully occupied (Supplementary Note 1, Fig. S3), which results in a blocking of the $t_{2g}-t_{2g}$ magnetic super-exchange channels. This leads to an almost negligible modification in the lattice parameters of the optimized structure with respect to the crystallographic non-magnetic one.

Resonance frequency changes due to spontaneous magnetostrictive strain

The predicted anisotropic change of lattice parameters when going from the paramagnetic to the AF phase, causes compressive stress, σ_a , and tensile stress, σ_b , along the a axis and b axis respectively, as illustrated in Fig. 1a, bottom panel. To quantify this anisotropy appearing at the phase transition, we use rectangular membranes, shown in Fig. 2b, to nanomechanically probe stress varia-

SUPPLEMENTARY TABLE 1. CoPS₃, FePS₃ and NiPS₃ lattice parameters of the crystallographic non-magnetic (NM) and fully optimized zigzag antiferromagnetic (AF-zigzag) configurations, as calculated by DFT (see Supplementary Note 1).

Lattice parameter (Å)	CoPS ₃		FePS ₃		NiPS ₃	
	<i>a</i>	<i>b</i>	<i>a</i>	<i>b</i>	<i>a</i>	<i>b</i>
NM	5.895	10.19	5.947	10.301	5.812	10.07
AF-zigzag	5.745	10.231	5.868	10.338	5.817	10.061
Change (%)	-2.545	+0.402	-1.328	+0.359	+0.086	-0.089

tions, along a specific crystallographic axis [21] (see Supplementary Note 2). In the following analysis, we neglect the stress contribution from the thermal expansion of the substrate, as this is small compared to that of the MPS₃ compounds [14].

The resonance frequency of the fundamental mode of a rectangular membrane, f_{res} , is approximately given by [22]:

$$f_{\text{res}} \approx \frac{1}{2} \sqrt{\frac{1}{\rho} \left[\frac{1}{w^2} \sigma_w + \frac{1}{l^2} \sigma_l \right]}, \quad (1)$$

where ρ is the mass density, w and l are respectively the width and length of the membrane, as indicated in Fig. 2b, and $\sigma_{w,l}$ are the stresses parallel to these directions. For high-aspect-ratio membranes ($w \ll l$), the mechanical resonance frequency is mostly determined by the stress along the shortest direction, σ_w .

We study the resonance frequency of thin MPS₃ flakes suspended over star-shaped cavities with 30° angular resolution, as shown in an example device in Fig. 2b. When the longest side of the cavity is aligned along a crystallographic axis (a or b) and $w \ll l$, its fundamental resonance frequency (f_a or f_b) is determined by the stress along the perpendicular axis (σ_b or σ_a):

$$f_a \approx \frac{1}{2} \sqrt{\frac{1}{\rho w^2} \sigma_b} \quad \text{and} \quad f_b \approx \frac{1}{2} \sqrt{\frac{1}{\rho w^2} \sigma_a}. \quad (2)$$

On cavities oriented at an intermediate angle, θ , (defined with respect to the b axis), the resonance frequency is:

$$f_\theta(T) \approx \frac{1}{2} \sqrt{\frac{1}{\rho w^2} \left[\sigma_{a,\theta} + \sigma_{b,\theta} \right]}, \quad (3)$$

$$\sigma_{a,\theta} = \frac{E}{(1-\nu^2)} (\cos^2 \theta + \nu \sin^2 \theta) (\bar{\epsilon} - \epsilon_{\text{ms},a}),$$

$$\sigma_{b,\theta} = \frac{E}{(1-\nu^2)} (\sin^2 \theta + \nu \cos^2 \theta) (\bar{\epsilon} - \epsilon_{\text{ms},b}),$$

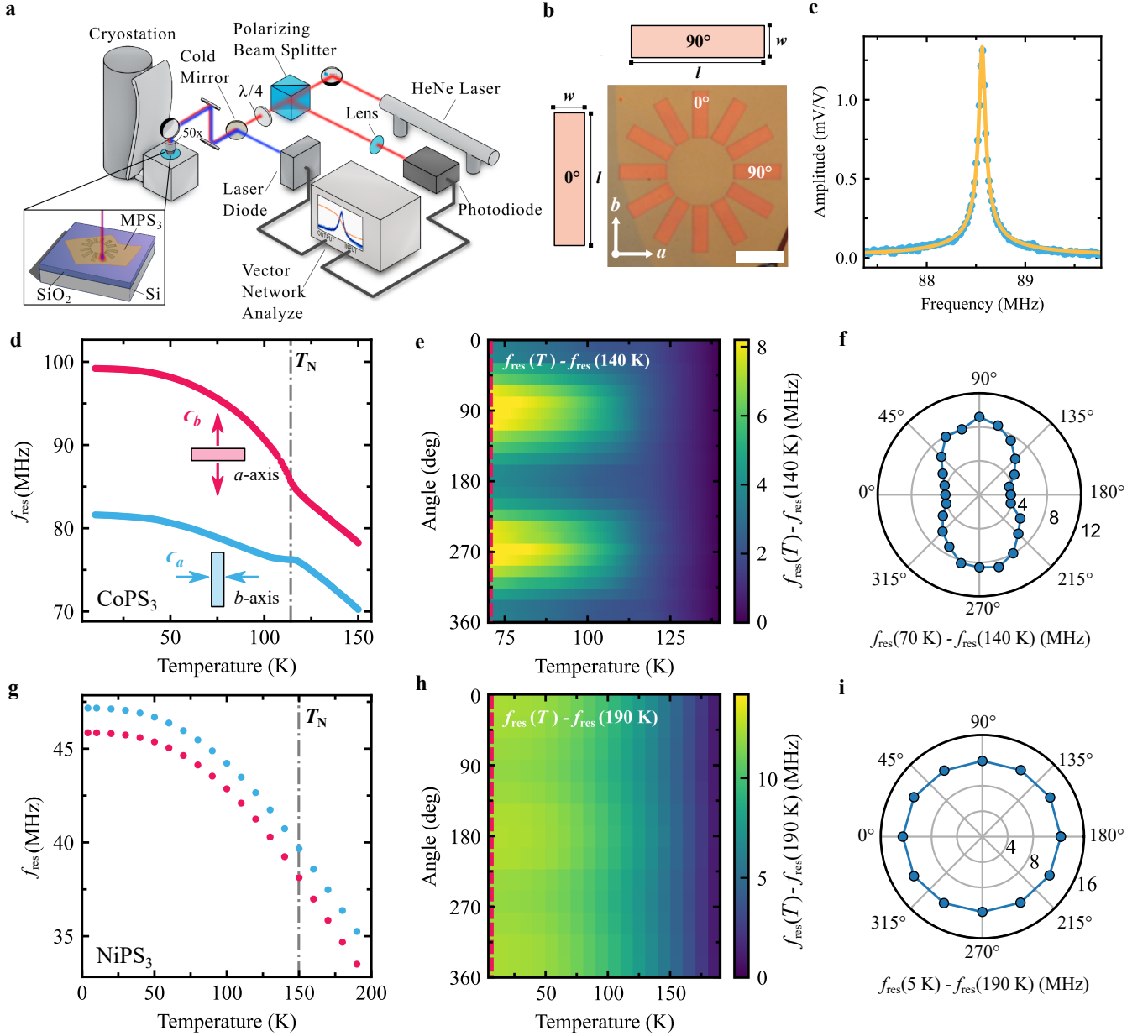
where we have used the constitutive equations for a magnetostrictive membrane with plane stress [23], while only keeping the anisotropy in the magnetostriction coefficient, Supplementary Note 2. Here, E is the Young's modulus and ν is Poisson's ratio of the material. Moreover, we have $\bar{\epsilon} = \epsilon_{\text{fab}} - \epsilon_{\text{th}}$, with ϵ_{fab} the residual fabrication strain and ϵ_{th} the phononic thermal expansion induced strain variation. The magnetostrictive strain along

the a and b -axes is given by $\epsilon_{\text{ms},a,b} = \lambda_{a,b} L^2$, respectively (see Supplementary Note 3 for a detailed derivation of Eq. (3)), where $\lambda_{a,b}$ are magnetostriction coefficients and L^2 is the AF order parameter squared.

The temperature dependence of the resonance frequency comprises two contributions: one due to the phononic thermal expansion coefficient α , given by $\epsilon_{\text{th}}(T) = \int_{T_0}^T \alpha(\tilde{T}) d\tilde{T}$, where T_0 is a reference temperature and \tilde{T} the integration variable, and the magnetostrictive contribution $\epsilon_{\text{ms},a,b}(T) = \lambda_{a,b} L^2(T)$. The former contribution is a slowly varying function of T , while the latter term contains the staggered magnetization, which increases abruptly near the phase transition; it thus can be used to determine $L(T)$, as we will show below. We assume $\lambda_{a,b}$ to be T independent, as its temperature dependence will be negligible when compared to that of $L(T)$.

Nanomechanical determination of the order parameter

To quantify the anisotropy in the magnetic membranes, a laser interferometry technique is used to measure their resonance frequency as a function of temperature [24]. A MPS₃ flake, suspended over holes in a patterned Si/SiO₂ chip, Fig. 2b, is placed inside a cryostat with optical access as shown in Fig. 2a. Both actuation and detection are done optically, by means of a power-modulated blue laser which opto-thermally excites the fundamental resonance, and a constant red laser which measures the change in the reflected signal resulting from the membrane's motion [14]. A typical resonance is shown in Fig. 2c, along with the damped harmonic oscillator model fit defining the resonance frequency. Figure 2d shows that in CoPS₃ f_a and f_b exhibit a similar temperature dependence for $T > T_N$, while opposite behaviour below the phase transition is visible, namely an increase of f_a and a relative decrease of f_b . This sudden change in $f(T)$ for the perpendicular cavities, occurring near T_N , constitutes, in accordance with the DFT calculations, the central result of this work as it shows that the magnetic ordering in MPS₃ leads to anisotropic strain and thus spontaneous magnetostriction. We further note that strictly speaking, T_N should be replaced by T_N^* which includes the effects of strain (see Supplementary Note 2).

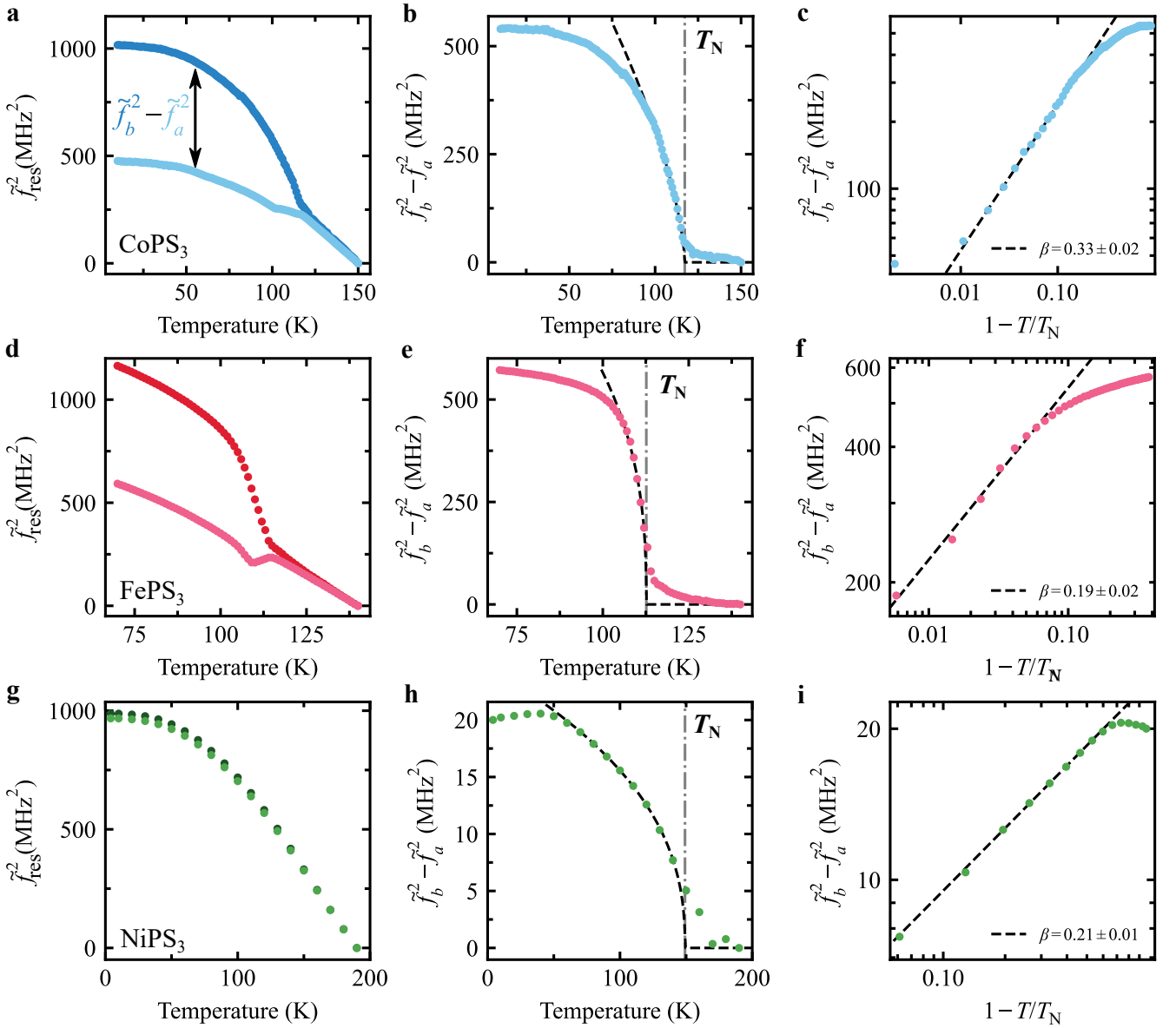


SUPPLEMENTARY FIG. 2. Angle-resolved mechanical characterization via laser interferometry. **a**, Schematic illustration of the laser interferometry setup and sample with rectangular cavity array. **b**, Optical image of the rectangular membranes array for a CoPS₃ sample. The a and b axis are determined from the resonance frequency behaviour. Scale bar: 12 μm . Schematic of 0° and 90° membranes from the array where w is the width of the membrane and l its length. **c**, Measured amplitude of the fundamental resonance peak in a CoPS₃ drum at $T = 10$ K and Lorentzian fit used to extract the fundamental resonance frequency, f_{res} , and quality factor, Q . **d**, Temperature dependence of f_{res} of a CoPS₃ rectangular membrane orientated along the a and b axes. The dashed line indicates the transition temperature T_N extracted from the data. **e**, Resonance frequency difference, $f_{\text{res}}(T) - f_{\text{res}}(140 \text{ K})$, as a function of angle and temperature. The dashed line indicates the transition as in **d**. **f**, Polar plot of $f_{\text{res}}(T) - f_{\text{res}}(140 \text{ K})$ taken along the red dashed line in **e**. Panels **g-i**, follow the same structure as **(c-e)** for NiPS₃ resonators with negligible anisotropy, measured between 5 K and 190 K.

For simplicity, we here use the notation T_N for the measured transition temperatures.

The anisotropic behavior of CoPS₃ in the AF state is even more evident in Fig. 2e, where $f_{\text{res}}(T) - f_{\text{res}}(140 \text{ K})$ for the different cavities of the star-shaped sample are plotted as a function of θ and temperature. The po-

lar plot in Fig. 2f shows the data along the red dashed line at $T = 70 \text{ K}$ in Fig. 2e and results in a characteristic dumbbell-shape. Similar anisotropic behaviour is observed in FePS₃ as shown in Supplementary Note 4. On the contrary, for NiPS₃ negligible anisotropy is observed in the angle-resolved magnetostriction data in Fig. 2g-i.



SUPPLEMENTARY FIG. 3. **Anisotropy and critical behaviour in resonance frequency of MPS₃ (M(II) = Co, Fe, Ni) membranes.** **a**, Pretension corrected resonance frequency ($\tilde{f}_a^2(T) = f_a^2(T) - f_a^2(150\text{K})$ and $\tilde{f}_b^2(T) = f_b^2(T) - f_b^2(150\text{K})$) of rectangular membranes of CoPS₃ oriented along the b axis (blue) and a axis (red) **b**, Difference of the corrected frequency squared $\tilde{f}_b^2 - \tilde{f}_a^2$ proportional to the order parameter L^2 from Eq. 4. The dashed-dotted line indicates the measured transition temperature T_N . The dashed black line is a powerlaw fit through the data close to T_N (see Supplementary Note 6). **c**, Difference of the corrected frequency squared $\tilde{f}_b^2 - \tilde{f}_a^2$ as a function of the reduced temperature $1 - T/T_N$. The dashed black line is the fit from **b** where the slope defines the critical exponent 2β . **d-f**, and **g-i**, follow the same structure as (a-d) for FePS₃ and NiPS₃ resonators, respectively.

To obtain $L(T)$ from the data, we first subtract the pretension contribution from the resonance frequency $f_\theta(T_0)$ by calculating $\tilde{f}_\theta^2(T) = f_\theta^2(T) - f_\theta^2(T_0)$, for each angle, where $T_0 = 150$ K is the highest temperature in our measurements. The resulting values of $\tilde{f}_\theta^2(T)$ along the crystalline axes a and b are shown in Fig. 3a,d,g for the three MPS₃ compounds. With Eq. (3), we then calculate the

difference $\tilde{f}_b^2(T) - \tilde{f}_a^2(T)$ which yields

$$\tilde{f}_b^2 - \tilde{f}_a^2 = \frac{E}{4\rho\omega^2(1+\nu)} [\lambda_a - \lambda_b] L^2. \quad (4)$$

We can now use Eq. (4) to access the critical behaviour of L below T_N by plotting $\tilde{f}_b^2 - \tilde{f}_a^2$ as a function of temperature. As shown in Fig. 3b,e,h, the trend presents the typical critical behaviour with a non-zero order pa-

parameter appearing in the ordered state for $T < T_N$. Figures 3c,f,i show the same critical curve as Fig. 3b,e,h respectively, plotted on a logarithmic scale against the reduced temperature $(1 - T/T_N)$. Note that the difference $\tilde{f}_b^2 - \tilde{f}_a^2$ for NiPS₃, is substantially smaller than that of the Fe/CoPS₃ membranes indicative of a weaker anisotropic magnetostrictive behaviour.

The angle dependence of the resonance frequencies allows us to estimate the ratio $r_{ab} = \lambda_a/\lambda_b$ between the magnetostriction parameters, $\lambda_{a,b}$, (see Supplementary Note 3). This ratio we directly compare to DFT calculations: Experimentally, we find for FePS₃, $r_{ab} = -2.3 \pm 0.3$ while from the DFT calculations we estimate $r_{ab} = -3.70$. For CoPS₃ (taking [25] $\nu_{\text{CoPS}_3} = 0.293$), the experimental value is -1.42 ± 0.07 and the DFT one -6.33 . We conclude that although both the sign and order of magnitude of the magnetostrictive anisotropy in these compounds are well reproduced in the current work, more detailed studies will be needed to obtain full quantitative correspondence with theory.

Thickness dependence of critical behaviour

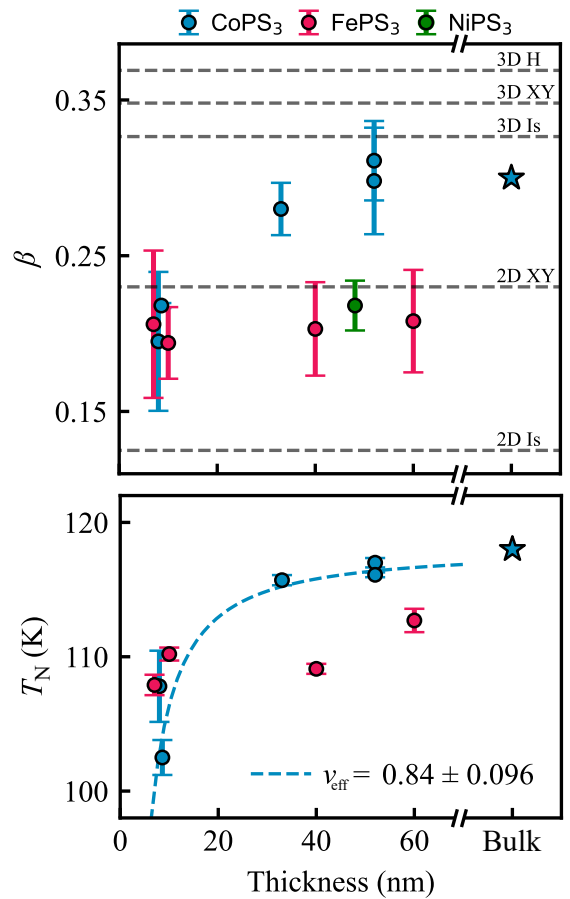
As follows from Landau's theory of phase transitions (see Supplementary Note 2), $L(T)$ near T_N is given by

$$L^2(T) = \begin{cases} 0 & \text{if } T > T_N \\ \frac{A}{2B}(T_N - T)^{2\beta} & \text{if } T < T_N, \end{cases} \quad (5)$$

where A and B are constants and β is a critical exponent representative of the magnetic order. We fit Eq. (5) to the data in Fig. 3b,e,h in the region close to T_N (indicated by the black dashed line in Fig. 3b,e,h) to extract the critical exponent β and T_N for the three materials (see Supplementary Note 6 for more details on the fitting procedure). In the logarithmic plot of the critical curve the fitting of a straight line shows good agreement to the data points, consistent with the result of Eq. (5). The values for β and T_N are plotted in Fig. 4 as a function of thickness, t , and listed in Supplementary Note 6, Table 49.

For the weakly anisotropic NiPS₃, $\beta = 0.218 \pm 0.016$, comparable to the value ($\beta = 0.22 \pm 0.02$) found in Ref. [27], and consistent with the expected 2D XY magnetic dimensionality ($\beta_{2\text{DXY}} = 0.233$) of NiPS₃ [28]. For FePS₃ we find $\beta = 0.208 \pm 0.033$, comparable with literature values [29]. For both β and T_N no appreciable thickness dependence is observed, similar to what has previously been reported in Ref. [30], where changes in the critical behaviour mostly become visible in the monolayer limit.

For thicker CoPS₃ samples ($t = 40 - 60$ nm) we find $\beta = 0.289 \pm 0.034$ close to what is reported in literature for the bulk ($\beta_{\text{bulk}} = 0.3 \pm 0.01$ [18]) and consistent with the 3D Ising model. For samples with $t < 10$ nm the measured β , on the other hand, is 0.195 ± 0.045 , closer



SUPPLEMENTARY FIG. 4. Thickness dependence of critical behaviour. Average critical exponent, β , and critical temperature, T_N , of MPS₃ resonators plotted as a function of thickness. The blue stars indicate CoPS₃ bulk values from [26]. Critical parameters have been determined from power law fits to $\tilde{f}_b^2 - \tilde{f}_a^2$, as shown in Fig. 3b,e,h, and then taking the average value over the fit parameter for all angles $\theta \neq 0$. Error bars are calculated from standard deviation of fit results for all θ . The horizontal gray dashed lines in the upper plot indicate the expected values of β for the 3D or 2D versions of the Heisenberg (H), XY or Ising (Is) models. The blue dashed line in the lower panel indicates a fit to Eq. (6) through the CoPS₃ data with $\nu_{\text{eff}} = 0.84 \pm 0.13$.

to $\beta_{2\text{DXY}}$ as shown in the top panel of Fig. 4. This constitutes a noticeable change in β while going from bulk to thinner samples. Similarly, we observe for CoPS₃ a decrease in T_N from the bulk value of 118 K down to ~ 100 K, similar to what was previously reported in Ref. [26]. We fit a power law to the dependence of T_N on thickness,

$$T_N(t)/T_N^{3\text{D}} \propto 1 - (C/t)^{1/\nu_{\text{eff}}}, \quad (6)$$

where C is a non-universal constant related to the interlayer coupling, and ν_{eff} is an effective critical exponent related to the correlation length [31]. Fitting the CoPS₃ data points with $T_N^{3\text{D}} = 118$ K [26] yields $C = 1.43 \pm 0.457$ nm and $\nu_{\text{eff}} = 0.84 \pm 0.096$. This

value of ν_{eff} is intermediate between the expected values of $\nu_{\text{eff}} = 0.630$ for the 3D Ising and $\nu_{\text{eff}} = 1$ for the 2D Ising models, and indicative of a transition regime [32].

CONCLUSIONS

In conclusion, we provide a comprehensive analysis of the anisotropic magnetostriction effect in MPS_3 compounds and its implications to the dynamics of membrane made from them. DFT calculations provide a microscopic explanation for the anisotropic lattice deformation in CoPS_3 , FePS_3 and NiPS_3 which are consistent with our measurements. We further demonstrate the relation between magnetic ordering and anisotropy in the mechanical resonance frequency of suspended MPS_3 resonators, providing a direct measure of the AF order parameter in absence of an external magnetic field. We observe a thickness dependence in the critical behaviour of CoPS_3 resonators [18, 26], which is absent in the case of FePS_3 . The presented technique is of particular interest for the study of 2D magnetism given the scarcity of methods available to investigate critical phenomena of van der Waals materials in the atomically thin limit.

METHODS

Sample fabrication. Substrates consist of thermal SiO_2 of 285 nm thickness, grown on highly doped (Si^{++}) silicon. The rectangular cavities are defined via e-beam lithography using AR-P 6200 resist. After development, the exposed SiO_2 areas are fully etched via reactive ion etching. The AR-P 6200 resist is stripped in PRS-3000 and the sample is cleaned in an O_2 plasma before stamping. The exfoliation and transfer of multi-layer MPS_3 flakes is done using a polydimethylsiloxaan (PDMS) transfer method. First, MPS_3 crystals are exfoliated onto the PDMS through scotch tape. Selected flakes are then transferred on the star-shaped cavities in the SiO_2/Si substrate.

Laser interferometry. Samples are mounted on a heater stage which is cooled down to 4 K using a Montana Instruments Cryostation s50 cryostat with optical access. A blue diode laser ($\lambda = 405$ nm) is used to excite the membrane optothermally via AC power-modulation from a vector network analyzer (VNA) [33]. Displacements are detected by focusing a red He-Ne laser beam ($\lambda = 632$ nm) on the cavity formed by the membrane and Si substrate. The reflected light, which is modulated by the position-dependent membrane motion, is recorded by a photodiode and processed by a phase-sensitive VNA. Laser spot size is $\sim 1 \mu\text{m}$.

DFT calculations. First principles spin-polarized DFT calculations in the plane wave formalism are performed as implemented in the Quantum ESPRESSO

package [34]. The exchange-correlation energy is calculated using the generalized gradient approximation using the Perdew–Burke–Ernzerhof functional [35] and standard Ultra-soft (USPP) solid-state pseudopotentials. The electronic wave functions are expanded with well-converged kinetic energy cut-offs for the wave functions (charge density) of 75 (800), 85 (800) and 85 (800) Ry for Fe, Co and Ni, respectively. The crystal structures are fully optimized using the Broyden–Fletcher–Goldfarb–Shanno (BFGS) algorithm [36] until the forces on each atom are smaller than 1×10^{-3} Ry/au and the energy difference between two consecutive relaxation steps is less than 1×10^{-4} Ry. In order to avoid unphysical interactions between images along the non-periodic direction, we add a vacuum of 18 Å in the z direction for the monolayer calculations. The Brillouin zone is sampled by a fine Γ -centered $5 \times 5 \times 1$ k -point Monkhorst–Pack [37]. A tight-binding Hamiltonian derived from first-principles is constructed in the base of Maximally-localized Wannier functions, as implemented in the Wannier90 code [38]. For that, we select the d orbitals of the metal centre (Fe, Co, Ni) and the s and p orbitals of P and S to construct the connected subspace. Magnetic interactions are determined using the Green’s function method in the TB2J software [39]. The orbital resolved analysis is performed after rotating the coordinate system of the crystal to align the metal-sulfur bonds direction of the octahedra with the cartesian axes.

Crystal growth Crystal growth of MPS_3 ($\text{M}(\text{II}) = \text{Ni, Fe, Co}$) is performed following a solid-state reaction inside a sealed evacuated quartz tube (pressure $\sim 5 \times 10^{-5}$ mbar). I_2 was used as a transport agent to obtain large crystals. A three-zone furnace is used, where a tube with the material was placed in the leftmost zone. This side is then heated up to 700 °C in 3 hours so that a temperature gradient of 700/650/675 °C is established. The other two zones are heated up in 24 hours from room temperature to 650 °C and kept at that temperature for one day. The temperature is kept constant for 28 days and cooled down naturally. With this process crystals with a length up to several centimeters are obtained. Detailed description of the crystal growth and characterization can be found in earlier work [14].

Data availability

All data supporting the findings of this article and its Supplementary Information will be made available upon request to the authors.

Acknowledgments

M.Š., M.J.A.H., G.B., M.L., H.S.J.v.d.Z. and P.G.S. acknowledge funding from the European Union’s Hori-

zon 2020 research and innovation program under grant agreement number 881603. Y.M.B and H.S.J.v.d.Z. acknowledge support from Dutch National Science Foundation (NWO). D.L.E., A.M.R., S.M.-V., C.B.-C., J.J.B., E.C. acknowledge funding from the European Union (ERC AdG Mol-2D 788222, ERC StG 2D-SMARTiES 101042680 and FET OPEN SINFONIA 964396), the Spanish MCIN (Project 2DHETEROS PID2020-117152RB-100 and Excellence Unit "Maria de Maeztu" CEX2019-000919 -M), the Spanish MIU (FPU21/04195 to A.M.R.) and the Generalitat Valenciana (PROMETEO Program and APOST Grant CIAPOS/2021/215 to S.M.-V.) The computations were performed on the Tirant III cluster of the Servei d'Informàtica of the University of Valencia.

Author contributions

D.L.E., A.M.R. performed the DFT and orbital resolved tight-binding calculations, supervised by J.J.B. M.Š., M.J.A.H. and G.B. performed the laser interferometry measurements and fabricated and inspected the samples. M.L. and M.J.A.H. fabricated the substrates. S.M.-V., C.B.-C. and E.C. synthesized and characterized the FePS₃, CoPS₃ and NiPS₃ crystals, supervised by E.c. M.Š., M.J.A.H. and G.B. analysed the experimental data. M.Š., M.J.A.H., Y.M.B., and P.G.S. modeled the experimental data. H.S.J.v.d.Z. and P.G.S. supervised the project. The paper was jointly written by all authors with a main contribution from M.J.A.H. All authors discussed the results and commented on the paper.

Competing interests

The authors declare no competing interests.

-
- [1] Mak, K. F., Shan, J. & Ralph, D. C. Probing and controlling magnetic states in 2D layered magnetic materials. *Nat. Rev. Phys.* **1**, 646–661 (2019).
- [2] Huang, B. *et al.* Layer-dependent ferromagnetism in a van der Waals crystal down to the monolayer limit. *Nature* **546**, 270–273 (2017).
- [3] Gong, C. *et al.* Discovery of intrinsic ferromagnetism in two-dimensional van der Waals crystals. *Nature* **546**, 265–269 (2017).
- [4] Lee, J.-U. *et al.* Ising-type magnetic ordering in atomically thin FePS₃. *Nano Lett.* **16**, 7433–7438 (2016).
- [5] Telford, E. J. *et al.* Layered antiferromagnetism induces large negative magnetoresistance in the van der Waals semiconductor CrSBr. *Adv. Mater.* **32**, 2003240 (2020).
- [6] Nēmec, P., Fiebig, M., Kampfrath, T. & Kimel, A. V. Antiferromagnetic opto-spintronics. *Nat. Phys.* **14**, 229–241 (2018).
- [7] Rahman, S., Torres, J. F., Khan, A. R. & Lu, Y. Recent developments in van der Waals antiferromagnetic 2D materials: Synthesis, characterization, and device implementation. *ACS Nano* **15**, 17175–17213 (2021).
- [8] Mertens, F. *et al.* Ultrafast coherent THz lattice dynamics coupled to spins in the van der Waals antiferromagnet FePS₃. *Adv. Mater.* 2208355 (2022).
- [9] Boix-Constant, C. *et al.* Probing the spin dimensionality in single-layer CrSBr van der Waals heterostructures by magneto-transport measurements. *Adv. Mater.* **34**, 2204940 (2022).
- [10] Esteras, D. L., Rybakov, A., Ruiz, A. M. & Baldoví, J. J. Magnon straintronics in the 2D van der Waals ferromagnet CrSBr from first-principles. *Nano Lett.* **22**, 8771–8778 (2022).
- [11] Wang, Y. *et al.* Strain-sensitive magnetization reversal of a van der Waals magnet. *Adv. Mater.* **32**, 2004533 (2020).
- [12] Ni, Z. *et al.* Imaging the Néel vector switching in the monolayer antiferromagnet MnPSe₃ with strain-controlled Ising order. *Nat. Nanotechnol.* **16**, 782–787 (2021).
- [13] Cenker, J. *et al.* Reversible strain-induced magnetic phase transition in a van der Waals magnet. *Nat. Nanotechnol.* 1–6 (2022).
- [14] Šiškins, M. *et al.* Magnetic and electronic phase transitions probed by nanomechanical resonators. *Nat. Commun.* **11**, 2698 (2020).
- [15] Šiškins, M. *et al.* Nanomechanical probing and strain tuning of the Curie temperature in suspended Cr₂Ge₂Te₆-based heterostructures. *npj 2D Mater. Appl.* **6**, 41 (2022).
- [16] Jiang, S., Xie, H., Shan, J. & Mak, K. F. Exchange magnetostriction in two-dimensional antiferromagnets. *Nat. Mater.* **19**, 1295–1299 (2020).
- [17] Chittari, B. L. *et al.* Electronic and magnetic properties of single-layer MPX₃ metal phosphorous trichalcogenides. *Phys. Rev. B* **94** (2016).
- [18] Wildes, A. R., Simonet, V., Ressouche, E., Ballou, R. & McIntyre, G. J. The magnetic properties and structure of the quasi-two-dimensional antiferromagnet CoPS₃. *J. Phys. Condens. Matter.* **29**, 455801 (2017).
- [19] Joy, P. A. & Vasudevan, S. Magnetism in the layered transition-metal thiophosphates MPS₃ (M=Mn, Fe, and Ni). *Phys. Rev. B* **46**, 5425–5433 (1992).
- [20] Takano, Y. *et al.* Magnetic properties and specific heat of MPS₃ (M=Mn, Fe, Zn). *J. Magn. Magn. Mat.* **272-276**, E593–E595 (2004).
- [21] Šiškins, M. *et al.* Highly anisotropic mechanical and optical properties of 2D layered As₂S₃ membranes. *ACS Nano* **13**, 10845–10851 (2019).
- [22] Leissa, A. W. & Qatu, M. S. *Vibrations of continuous systems* (New York: McGraw-Hill, 2011).
- [23] Landau, L. D., Pitaevskii, L. P. & Lifshitz, E. M. *Electrodynamics of continuous media*, vol. 8 (Butterworth, New York, 1984), 2 edn.

- [24] Bunch, J. S. *et al.* Electromechanical resonators from graphene sheets. *Science* **315**, 490–493 (2007).
- [25] Gui, Q. *et al.* Extrinsic-structured bimetallic-phase ternary metal phosphorus trisulfides coupled with n-doped graphitized carbon for superior electrochemical lithium storage. *Adv. Energy Mater.* **11**, 2003553 (2021).
- [26] Liu, Q. *et al.* Magnetic order in XY-type antiferromagnetic monolayer CoPS₃ revealed by Raman spectroscopy. *Phys. Rev. B* **103**, 235411 (2021).
- [27] Afanasiev, D. *et al.* Controlling the anisotropy of a van der Waals antiferromagnet with light. *Sci. Adv.* **7**, eabf3096 (2021).
- [28] Kim, K. *et al.* Suppression of magnetic ordering in XXZ-type antiferromagnetic monolayer NiPS₃. *Nat. Commun.* **10**, 345 (2019).
- [29] Yao-Dong, D. *et al.* A Mössbauer study of the magnetic coupling in iron phosphorous trisulfides. *Chinese Phys.* **13**, 1652 (2004).
- [30] Zhang, Q. *et al.* Observation of giant optical linear dichroism in a zigzag antiferromagnet FePS₃. *Nano Lett.* **8** (2021).
- [31] Zhang, R. & Willis, R. F. Thickness-dependent Curie temperatures of ultrathin magnetic films: Effect of the range of spin-spin interactions. *Phys. Rev. Lett.* **86**, 2665–2668 (2001).
- [32] Gibertini, M., Koperski, M., Morpurgo, A. F. & Novoselov, K. S. Magnetic 2D materials and heterostructures. *Nat. Nanotechnol.* **14**, 408–419 (2019).
- [33] Steeneken, P. G., Dolleman, R. J., Davidovikj, D., Alijani, F. & van der Zant, H. S. J. Dynamics of 2D material membranes. *2D Mater.* **8**, 042001 (2021).
- [34] Giannozzi, P. *et al.* QUANTUM ESPRESSO: a modular and open-source software project for quantum simulations of materials. *J. Phys. Condens. Matter* **21**, 395502 (2009).
- [35] Perdew, J. P., Burke, K. & Ernzerhof, M. Generalized gradient approximation made simple. *Phys. Rev. Lett.* **77**, 3865–3868 (1996).
- [36] Head, J. D. & Zerner, M. C. A Broyden—Fletcher—Goldfarb—Shanno optimization procedure for molecular geometries. *Chem. Phys. Lett.* **122**, 264–270 (1985).
- [37] Monkhorst, H. J. & Pack, J. D. Special points for Brillouin-zone integrations. *Phys. Rev. B* **13**, 5188–5192 (1976).
- [38] Mostofi, A. A. *et al.* wannier90: A tool for obtaining maximally-localised wannier functions. *Comput. Phys. Commun.* **178**, 685–699 (2008).
- [39] He, X., Helbig, N., Verstraete, M. J. & Bousquet, E. Tb2j: A python package for computing magnetic interaction parameters. *Comput. Phys. Commun.* **264**, 107938 (2021).

SUPPLEMENTARY INFORMATION: Magnetic order in 2D antiferromagnets revealed by spontaneous anisotropic magnetostriction

Maurits J. A. Houmes,^{4,*} Gabriele Baglioni,^{4,*} Makars Šiškins,^{4,*} Martin Lee,⁴ Dorye L. Esteras,⁵ Alberto M. Ruiz,⁵ Samuel Mañas-Valero,^{4,5} Carla Boix-Constant,⁵ Jose J. Baldoví,⁵ Eugenio Coronado,⁵ Yaroslav M. Blanter,⁴ Peter G. Steeneken,^{4,6} and Herre S. J. van der Zant⁴

⁴*Kavli Institute of Nanoscience, Delft University of Technology, Lorentzweg 1,
2628 CJ, Delft, The Netherlands*

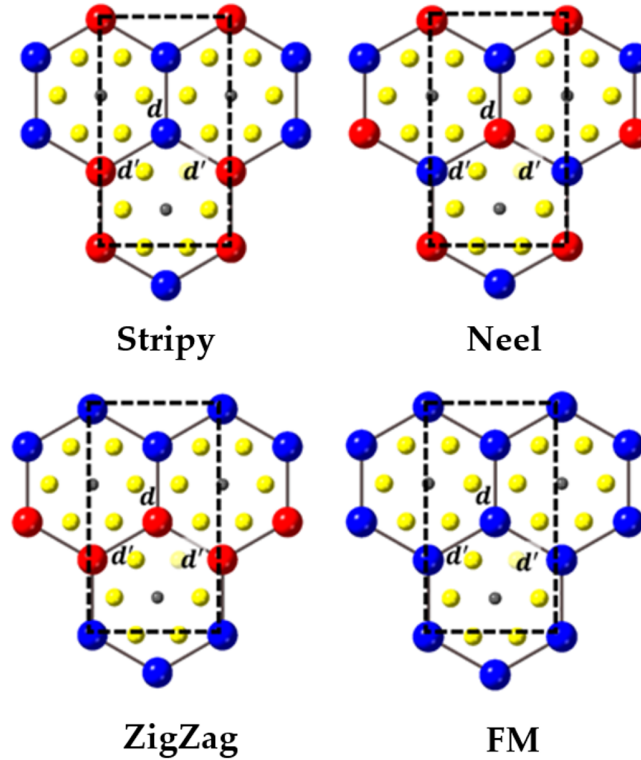
⁵*Instituto de Ciencia Molecular (ICMol), Universitat de València, c/Catedrático José Beltrán 2,
46980 Paterna, Spain*

⁶*Department of Precision and Microsystems Engineering, Delft University of Technology, Mekelweg 2,
2628 CD, Delft, The Netherlands*

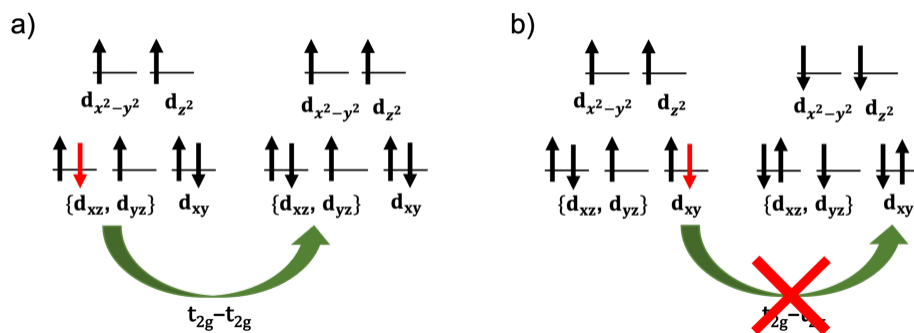
* These authors contributed equally.

Supplementary Note 1. DENSITY FUNCTIONAL THEORY CALCULATIONS

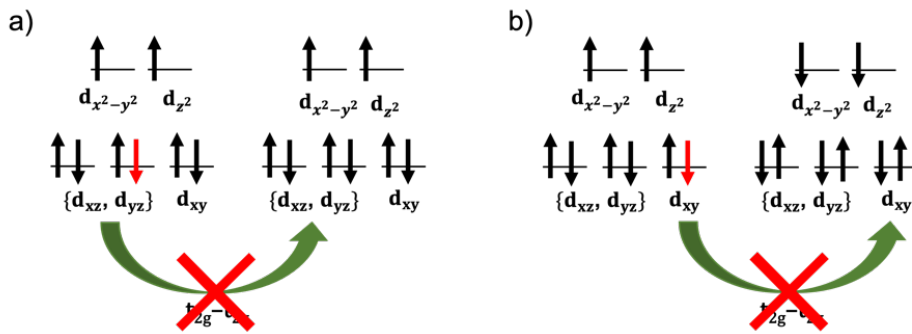
This section summarizes the results of orbital-resolved magnetic exchange analyses based on maximally localized Wannier functions, for both the crystallographic and optimized structures. These results are included in Supplementary Tables 7 – 42. Supplementary Tables 43 – 48 display the hopping integrals with the S atoms (Supplementary Fig. 8) that mediate the super-exchange interactions between magnetic centers for each channel.



SUPPLEMENTARY FIG. 5. Top view of a single-layer of MPS_3 for different magnetic configurations, namely stripy, Néel, zigzag and ferromagnetic (FM). Blue and red balls represent transition metal atoms with spin up and down components, respectively.



SUPPLEMENTARY FIG. 6. Electron configuration of the Co^{2+} magnetic ions connected by J_1 (a) and J_2 (b), showing parallel and antiparallel spin orientations, respectively. Green arrows illustrate the most relevant ferromagnetic superexchange channels, namely $d_{yz}-d_{yz}$ and $d_{xy}-d_{xy}$ (cancelled), for J_1 and J_2 respectively



SUPPLEMENTARY FIG. 7. Electron configuration of the Ni^{2+} magnetic ions connected by J_1 (a) and J_2 (b), showing parallel and antiparallel spin orientations, respectively. Green arrows illustrate the most relevant ferromagnetic superexchange channels, namely d_{yz} - d_{yz} (cancelled) and d_{xy} - d_{xy} (cancelled), for J_1 and J_2 respectively.

SUPPLEMENTARY TABLE 2. CoPS_3 , FePS_3 and NiPS_3 lattice parameters of the crystallographic non-magnetic (NM) and Stripy antiferromagnetic (AF) configurations

Lattice parameter (\AA)	CoPS_3		FePS_3		NiPS_3	
	a	b	a	b	a	b
Crystallographic NM	5.895	10.190	5.947	10.301	5.812	10.070
AF-stripy	5.772	10.003	5.978	10.172	5.826	10.084
Change (%)	-2.086	-1.835	+0.521	-1.252	+0.241	+0.139

SUPPLEMENTARY TABLE 3. CoPS_3 , FePS_3 and NiPS_3 lattice parameters of the crystallographic non-magnetic (NM) and Néel antiferromagnetic (AF) configurations.

Lattice parameter (\AA)	CoPS_3		FePS_3		NiPS_3	
	a	b	a	b	a	b
Crystallographic NM	5.895	10.190	5.947	10.301	5.812	10.070
AF-Néel	5.885	10.187	5.947	10.303	5.834	10.106
Change (%)	-0.169	-0.029	+0.000	+0.019	+0.378	+0.357

SUPPLEMENTARY TABLE 4. CoPS_3 , FePS_3 and NiPS_3 lattice parameters of the crystallographic non-magnetic (NM) and ferromagnetic (FM) configurations.

Lattice parameter (\AA)	CoPS_3		FePS_3		NiPS_3	
	a	b	a	b	a	b
Crystallographic NM	5.895	10.190	5.947	10.301	5.812	10.070
FM	5.836	10.103	5.932	10.278	5.824	10.089
Change (%)	-1.001	-0.854	-0.252	-0.223	+0.207	+0.189

SUPPLEMENTARY TABLE 5. CoPS_3 , FePS_3 and NiPS_3 distances (d and d') of the crystallographic non-magnetic (NM) and zigzag antiferromagnetic (AF) configurations.

Distance (\AA)	CoPS_3		FePS_3		NiPS_3	
	d	d'	d	d'	d	d'
Crystallographic NM	3.397	3.402	3.433	3.433	3.357	3.356
AF-zigzag	3.723	3.192	3.626	3.316	3.353	3.359
Change (%)	+9.596	-6.172	+5.621	-3.408	-0.119	+0.089

SUPPLEMENTARY TABLE 6. CoPS₃, FePS₃ and NiPS₃ distances (d and d') of the crystallographic non-magnetic (NM) and Stripy antiferromagnetic (AF) configurations.

Distance (Å)	CoPS ₃		FePS ₃		NiPS ₃	
	d	d'	d	d'	d	d'
Crystallographic NM	3.397	3.402	3.433	3.433	3.357	3.356
AF-stripy	3.337	3.332	2.670	3.843	3.373	3.357
Change (%)	-1.766	-2.058	-22.225	+11.943	+0.477	+0.029

SUPPLEMENTARY TABLE 7. CoPS₃, FePS₃ and NiPS₃ distances (d and d') of the crystallographic non-magnetic (NM) and Néel antiferromagnetic (AF) configurations.

Distance (Å)	CoPS ₃		FePS ₃		NiPS ₃	
	d	d'	d	d'	d	d'
Crystallographic NM	3.397	3.402	3.433	3.433	3.357	3.356
AF-Néel	3.393	3.398	3.436	3.433	3.369	3.369
Change (%)	-0.118	-0.118	+0.087	+0.000	+0.357	+0.387

SUPPLEMENTARY TABLE 8. CoPS₃, FePS₃ and NiPS₃ distances (d and d') of the crystallographic non-magnetic (NM) and ferromagnetic (FM) configurations.

Distance (Å)	CoPS ₃		FePS ₃		NiPS ₃	
	d	d'	d	d'	d	d'
Crystallographic NM	3.397	3.402	3.433	3.433	3.357	3.356
FM	3.368	3.368	3.429	3.424	3.363	3.362
Change (%)	-0.854	-0.999	+0.116	+0.262	+0.179	+0.179

SUPPLEMENTARY TABLE 9. Orbital resolved exchange parameters for the experimental structure of FePS₃.

J₁ (meV)	d_{z2}	d_{xz}	d_{yz}	d_{x2y2}	d_{xy}
d_{z2}	-0.467	-0.154	-0.157	-0.047	-0.027
d_{xz}	-0.154	7.091	0.063	-0.307	0.288
d_{yz}	-0.157	0.063	7.215	-0.103	0.109
d_{x2y2}	-0.047	-0.307	-0.103	-0.194	-0.017
d_{xy}	-0.027	0.288	0.109	-0.017	1.612

SUPPLEMENTARY TABLE 10. Orbital resolved exchange parameters for the experimental structure of FePS₃.

J₂ (meV)	d_{z2}	d_{xz}	d_{yz}	d_{x2y2}	d_{xy}
d_{z2}	-0.045	-0.013	-0.011	-0.008	-1.18
d_{xz}	-0.013	0.334	0.14	0.0	0.791
d_{yz}	-0.011	0.14	0.418	0.036	0.634
d_{x2y2}	-0.008	0.0	0.036	-0.783	0.086
d_{xy}	-1.18	0.791	0.634	0.086	11.016

SUPPLEMENTARY TABLE 11. Orbital resolved exchange parameters for the experimental structure of FePS₃.

J₃ (meV)	d_{z2}	d_{xz}	d_{yz}	d_{x2y2}	d_{xy}
d_{z2}	0.01	-0.058	-0.065	-0.028	-0.011
d_{xz}	-0.058	-0.02	-0.037	-0.101	-0.076
d_{yz}	-0.065	-0.037	-0.022	-0.122	0.089
d_{x2y2}	-0.028	-0.101	-0.122	-0.004	-0.041
d_{xy}	-0.011	-0.076	-0.089	-0.041	0.405

SUPPLEMENTARY TABLE 12. Orbital resolved exchange parameters for the experimental structure of FePS₃.

J₄ (meV)	d_{z2}	d_{xz}	d_{yz}	d_{x2y2}	d_{xy}
d_{z2}	-0.121	0.002	0.003	0.013	-0.234
d_{xz}	0.002	-0.093	-0.022	-0.005	-0.146
d_{yz}	0.003	-0.022	-0.081	0.002	0.122
d_{x2y2}	0.012	-0.005	0.002	-0.01	-0.18
d_{xy}	-0.234	-0.146	-0.122	-0.18	-2.509

SUPPLEMENTARY TABLE 13. Orbital resolved exchange parameters for the experimental structure of FePS₃.

J₅ (meV)	d_{z2}	d_{xz}	d_{yz}	d_{x2y2}	d_{xy}
d_{z2}	-2.323	0.019	0.015	-1.175	0.148
d_{xz}	0.019	0.035	0.024	-0.01	-0.239
d_{yz}	0.015	0.024	0.022	-0.032	0.154
d_{x2y2}	-1.175	-0.01	-0.032	-0.154	-0.138
d_{xy}	0.148	-0.239	-0.154	-0.138	-2.491

SUPPLEMENTARY TABLE 14. Orbital resolved exchange parameters for the experimental structure of FePS₃.

J₆ (meV)	d_{z2}	d_{xz}	d_{yz}	d_{x2y2}	d_{xy}
d_{z2}	-0.156	0.03	0.025	-0.0	-0.05
d_{xz}	0.03	-0.012	0.004	0.053	-0.073
d_{yz}	0.025	0.004	-0.01	0.04	0.042
d_{x2y2}	-0.0	0.053	0.04	-5.914	-0.044
d_{xy}	-0.05	-0.073	-0.042	-0.044	0.325

SUPPLEMENTARY TABLE 15. Orbital resolved exchange parameters for the spin polarized optimized structure of FePS₃.

J₁ (meV)	d_{z2}	d_{xz}	d_{yz}	d_{x2y2}	d_{xy}
d_{z2}	-0.899	-0.192	-0.188	-0.127	-0.017
d_{xz}	-0.192	8.323	0.035	-0.29	0.306
d_{yz}	-0.188	0.035	8.383	-0.088	0.12
d_{x2y2}	-0.127	-0.29	-0.088	-0.28	-0.044
d_{xy}	-0.017	0.306	0.12	-0.044	1.823

SUPPLEMENTARY TABLE 16. Orbital resolved exchange parameters for the spin polarized optimized structure of FePS₃.

J₂ (meV)	d_{z2}	d_{xz}	d_{yz}	d_{x2y2}	d_{xy}
d_{z2}	-0.104	-0.021	-0.019	-0.009	-2.114
d_{xz}	-0.021	0.161	0.019	-0.005	0.5
d_{yz}	-0.019	0.019	0.182	0.002	0.432
d_{x2y2}	-0.009	-0.005	0.002	0.128	0.015
d_{xy}	-2.114	0.5	0.432	0.015	5.022

SUPPLEMENTARY TABLE 17. Orbital resolved exchange parameters for the spin polarized optimized structure of FePS₃.

J₃ (meV)	d_{z2}	d_{xz}	d_{yz}	d_{x2y2}	d_{xy}
d_{z2}	0.012	-0.083	-0.093	-0.059	-0.013
d_{xz}	-0.083	-0.025	-0.044	-0.088	-0.059
d_{yz}	-0.093	-0.044	-0.027	-0.105	-0.064
d_{x2y2}	-0.059	-0.088	-0.105	0.007	-0.038
d_{xy}	-0.013	-0.059	-0.064	-0.038	0.278

SUPPLEMENTARY TABLE 18. Orbital resolved exchange parameters for the spin polarized optimized structure of FePS₃.

J₄ (meV)	d_{z2}	d_{xz}	d_{yz}	d_{x2y2}	d_{xy}
d_{z2}	-0.11	0.002	0.003	0.036	-0.212
d_{xz}	0.002	-0.112	-0.039	-0.014	-0.061
d_{yz}	0.003	-0.039	-0.105	0.0	-0.066
d_{x2y2}	0.036	-0.014	0.0	-0.004	-0.164
d_{xy}	-0.212	-0.061	-0.066	-0.164	-1.186

SUPPLEMENTARY TABLE 19. Orbital resolved exchange parameters for the spin polarized optimized structure of FePS₃.

J₅ (meV)	d_{z2}	d_{xz}	d_{yz}	d_{x2y2}	d_{xy}
d_{z2}	-2.613	-0.016	-0.014	-1.223	0.154
d_{xz}	-0.016	-0.008	0.032	-0.059	-0.105
d_{yz}	-0.014	0.032	-0.016	-0.075	-0.06
d_{x2y2}	-1.223	-0.059	-0.075	-0.181	-0.122
d_{xy}	0.154	-0.105	-0.06	-0.122	-1.114

SUPPLEMENTARY TABLE 20. Orbital resolved exchange parameters for the spin polarized optimized structure of FePS₃.

J₆ (meV)	d_{z2}	d_{xz}	d_{yz}	d_{x2y2}	d_{xy}
d_{z2}	-0.196	0.064	0.056	-0.001	-0.236
d_{xz}	0.064	-0.026	0.005	0.083	-0.092
d_{yz}	0.056	0.005	-0.022	0.083	-0.071
d_{x2y2}	-0.001	0.083	0.083	-5.386	-0.025
d_{xy}	-0.236	-0.092	-0.071	-0.025	1.036

SUPPLEMENTARY TABLE 21. Orbital resolved exchange parameters for the experimental structure of CoPS₃.

J₁ (meV)	d_{z2}	d_{xz}	d_{yz}	d_{x2y2}	d_{xy}
d_{z2}	0.168	-0.907	-0.922	0.108	-0.221
d_{xz}	-0.907	7.514	0.105	-0.977	-0.417
d_{yz}	-0.922	0.105	7.465	-1.266	-0.066
d_{x2y2}	0.108	-0.977	-1.266	-0.094	0.073
d_{xy}	-0.221	-0.417	-0.065	0.073	-0.36

SUPPLEMENTARY TABLE 22. Orbital resolved exchange parameters for the experimental structure of CoPS₃.

J₂ (meV)	d_{z2}	d_{xz}	d_{yz}	d_{x2y2}	d_{xy}
d_{z2}	-0.371	0.078	0.066	-0.002	-0.242
d_{xz}	0.078	0.524	0.022	0.115	-0.093
d_{yz}	0.066	0.022	0.54	-0.106	0.126
d_{x2y2}	-0.002	0.115	-0.106	-0.687	-0.034
d_{xy}	-0.242	-0.093	0.126	-0.034	-0.068

SUPPLEMENTARY TABLE 23. Orbital resolved exchange parameters for the experimental structure of CoPS₃.

J₃ (meV)	d_{z2}	d_{xz}	d_{yz}	d_{x2y2}	d_{xy}
d_{z2}	0.069	-0.117	-0.114	-0.047	-0.004
d_{xz}	-0.117	-0.06	-0.024	-0.326	-0.003
d_{yz}	-0.114	-0.024	-0.059	-0.367	0.01
d_{x2y2}	-0.047	-0.326	-0.367	-0.17	0.003
d_{xy}	-0.004	-0.003	0.01	0.004	-0.022

SUPPLEMENTARY TABLE 24. Orbital resolved exchange parameters for the experimental structure of CoPS₃.

\mathbf{J}_4 (meV)	\mathbf{d}_{z2}	\mathbf{d}_{xz}	\mathbf{d}_{yz}	\mathbf{d}_{x2y2}	\mathbf{d}_{xy}
\mathbf{d}_{z2}	-0.025	-0.011	-0.001	0.015	0.046
\mathbf{d}_{xz}	-0.011	-0.062	-0.004	0.002	0.047
\mathbf{d}_{yz}	-0.001	-0.004	-0.05	-0.006	0.046
\mathbf{d}_{x2y2}	0.015	0.002	-0.006	-0.082	-0.013
\mathbf{d}_{xy}	0.046	0.047	0.046	-0.013	0.055

SUPPLEMENTARY TABLE 25. Orbital resolved exchange parameters for the experimental structure of CoPS₃.

\mathbf{J}_5 (meV)	\mathbf{d}_{z2}	\mathbf{d}_{xz}	\mathbf{d}_{yz}	\mathbf{d}_{x2y2}	\mathbf{d}_{xy}
\mathbf{d}_{z2}	-3.482	-0.181	-0.163	-0.862	0.13
\mathbf{d}_{xz}	-0.181	-0.018	0.001	-0.263	0.034
\mathbf{d}_{yz}	-0.163	0.001	-0.044	-0.18	0.004
\mathbf{d}_{x2y2}	-0.862	-0.263	-0.18	-0.016	0.097
\mathbf{d}_{xy}	0.13	0.034	0.004	0.097	0.051

SUPPLEMENTARY TABLE 26. Orbital resolved exchange parameters for the experimental structure of CoPS₃.

\mathbf{J}_3 (meV)	\mathbf{d}_{z2}	\mathbf{d}_{xz}	\mathbf{d}_{yz}	\mathbf{d}_{x2y2}	\mathbf{d}_{xy}
\mathbf{d}_{z2}	-0.321	0.054	0.045	0.001	0.114
\mathbf{d}_{xz}	0.054	-0.018	-0.023	0.138	0.072
\mathbf{d}_{yz}	0.045	-0.023	-0.01	0.224	0.01
\mathbf{d}_{x2y2}	0.001	0.138	0.224	-3.745	-0.026
\mathbf{d}_{xy}	0.114	0.072	0.01	-0.026	0.029

SUPPLEMENTARY TABLE 27. Orbital resolved exchange parameters for the spin polarized optimized structure of CoPS₃.

\mathbf{J}_1 (meV)	\mathbf{d}_{z2}	\mathbf{d}_{xz}	\mathbf{d}_{yz}	\mathbf{d}_{x2y2}	\mathbf{d}_{xy}
\mathbf{d}_{z2}	-0.029	-0.889	-0.868	-0.449	-0.182
\mathbf{d}_{xz}	-0.889	10.043	0.01	-0.658	0.055
\mathbf{d}_{yz}	-0.868	0.01	10.011	-0.76	0.152
\mathbf{d}_{x2y2}	-0.449	-0.658	-0.76	0.024	-0.03
\mathbf{d}_{xy}	-0.182	0.055	0.152	-0.03	-0.173

SUPPLEMENTARY TABLE 28. Orbital resolved exchange parameters for the spin polarized optimized structure of CoPS₃.

\mathbf{J}_2 (meV)	\mathbf{d}_{z2}	\mathbf{d}_{xz}	\mathbf{d}_{yz}	\mathbf{d}_{x2y2}	\mathbf{d}_{xy}
\mathbf{d}_{z2}	-0.213	0.02	0.018	0.0	-0.113
\mathbf{d}_{xz}	0.02	0.106	-0.008	-0.014	0.122
\mathbf{d}_{yz}	0.018	-0.008	0.109	-0.038	0.128
\mathbf{d}_{x2y2}	0.0	-0.014	-0.038	-0.035	0.0
\mathbf{d}_{xy}	-0.113	0.122	0.128	0.0	-0.199

SUPPLEMENTARY TABLE 29. Orbital resolved exchange parameters for the spin polarized optimized structure of CoPS₃.

\mathbf{J}_3 (meV)	\mathbf{d}_{z2}	\mathbf{d}_{xz}	\mathbf{d}_{yz}	\mathbf{d}_{x2y2}	\mathbf{d}_{xy}
\mathbf{d}_{z2}	0.029	-0.135	-0.136	-0.162	-0.027
\mathbf{d}_{xz}	-0.135	-0.049	-0.018	-0.2	0.051
\mathbf{d}_{yz}	-0.136	-0.018	-0.049	-0.215	0.051
\mathbf{d}_{x2y2}	-0.162	-0.2	-0.215	-0.089	-0.007
\mathbf{d}_{xy}	-0.027	0.051	0.051	-0.007	0.011

SUPPLEMENTARY TABLE 30. Orbital resolved exchange parameters for the spin polarized optimized structure of CoPS₃.

J₄ (meV)	d_{z2}	d_{xz}	d_{yz}	d_{x2y2}	d_{xy}
d_{z2}	-0.014	0.002	0.005	0.068	-0.048
d_{xz}	0.002	-0.019	-0.027	-0.002	0.009
d_{yz}	0.005	-0.027	-0.014	-0.013	0.016
d_{x2y2}	0.068	-0.002	-0.013	-0.071	-0.021
d_{xy}	-0.048	0.009	0.016	-0.021	0.002

SUPPLEMENTARY TABLE 31. Orbital resolved exchange parameters for the spin polarized optimized structure of CoPS₃.

J₅ (meV)	d_{z2}	d_{xz}	d_{yz}	d_{x2y2}	d_{xy}
d_{z2}	-3.726	-0.232	-0.228	-1.283	0.014
d_{xz}	-0.232	-0.055	0.0	-0.211	0.002
d_{yz}	-0.229	0.0	-0.058	-0.183	-0.004
d_{x2y2}	-1.283	-0.211	-0.183	-0.06	0.002
d_{xy}	0.014	0.002	-0.004	0.002	0.002

SUPPLEMENTARY TABLE 32. Orbital resolved exchange parameters for the spin polarized optimized structure of CoPS₃.

J₆ (meV)	d_{z2}	d_{xz}	d_{yz}	d_{x2y2}	d_{xy}
d_{z2}	-0.483	0.099	0.087	0.001	0.316
d_{xz}	0.099	-0.068	0.0	0.08	0.064
d_{yz}	0.087	0.0	-0.066	0.108	0.041
d_{x2y2}	0.001	0.08	0.108	-3.258	-0.01
d_{xy}	0.316	0.064	0.041	-0.01	0.196

SUPPLEMENTARY TABLE 33. Orbital resolved exchange parameters for the experimental structure of NiPS₃.

J₁ (meV)	d_{z2}	d_{xz}	d_{yz}	d_{x2y2}	d_{xy}
d_{z2}	-0.055	-0.008	-0.012	-0.038	0.002
d_{xz}	-0.008	0.014	-0.002	0.011	0.001
d_{yz}	-0.012	-0.002	0.012	0.007	0.0
d_{x2y2}	-0.038	0.011	0.007	-0.312	-0.004
d_{xy}	0.003	0.001	0.0	-0.004	-0.002

SUPPLEMENTARY TABLE 34. Orbital resolved exchange parameters for the experimental structure of NiPS₃.

J₂ (meV)	d_{z2}	d_{xz}	d_{yz}	d_{x2y2}	d_{xy}
d_{z2}	-0.161	-0.012	-0.01	0.0	-0.011
d_{xz}	-0.012	-0.006	0.001	0.001	0.005
d_{yz}	-0.01	0.001	-0.006	0.001	0.005
d_{x2y2}	0.0	0.001	0.001	-0.1	-0.008
d_{xy}	-0.011	0.005	0.005	-0.008	0.017

SUPPLEMENTARY TABLE 35. Orbital resolved exchange parameters for the experimental structure of NiPS₃.

J₃ (meV)	d_{z2}	d_{xz}	d_{yz}	d_{x2y2}	d_{xy}
d_{z2}	0.015	-0.0	0.0	0.004	0.001
d_{xz}	-0.0	-0.0	-0.001	0.011	-0.0
d_{yz}	0.0	-0.001	-0.0	0.012	-0.0
d_{x2y2}	0.004	0.011	0.012	0.053	0.007
d_{xy}	0.001	-0.0	-0.0	0.007	-0.0

SUPPLEMENTARY TABLE 36. Orbital resolved exchange parameters for the experimental structure of NiPS₃.

\mathbf{J}_4 (meV)	\mathbf{d}_{z^2}	\mathbf{d}_{xz}	\mathbf{d}_{yz}	$\mathbf{d}_{x^2y^2}$	\mathbf{d}_{xy}
\mathbf{d}_{z^2}	0.204	-0.001	-0.0	0.024	0.003
\mathbf{d}_{xz}	-0.001	-0.001	0.0	-0.0	0.0
\mathbf{d}_{yz}	-0.0	0.0	-0.001	0.0	0.0
$\mathbf{d}_{x^2y^2}$	0.024	-0.0	0.0	-0.028	-0.009
\mathbf{d}_{xy}	0.003	0.0	0.0	-0.009	-0.001

SUPPLEMENTARY TABLE 37. Orbital resolved exchange parameters for the experimental structure of NiPS₃.

\mathbf{J}_5 (meV)	\mathbf{d}_{z^2}	\mathbf{d}_{xz}	\mathbf{d}_{yz}	$\mathbf{d}_{x^2y^2}$	\mathbf{d}_{xy}
\mathbf{d}_{z^2}	-5.191	-0.074	-0.061	-2.334	-0.042
\mathbf{d}_{xz}	-0.074	-0.006	-0.0	-0.031	0.0
\mathbf{d}_{yz}	-0.061	-0.0	-0.006	-0.024	-0.0
$\mathbf{d}_{x^2y^2}$	-2.334	-0.031	-0.024	-0.38	-0.003
\mathbf{d}_{xy}	-0.042	0.0	-0.0	-0.003	-0.001

SUPPLEMENTARY TABLE 38. Orbital resolved exchange parameters for the experimental structure of NiPS₃.

\mathbf{J}_6 (meV)	\mathbf{d}_{z^2}	\mathbf{d}_{xz}	\mathbf{d}_{yz}	$\mathbf{d}_{x^2y^2}$	\mathbf{d}_{xy}
\mathbf{d}_{z^2}	-0.058	-0.002	-0.002	0.0	0.028
\mathbf{d}_{xz}	-0.002	0.0	0.0	-0.003	0.0
\mathbf{d}_{yz}	-0.002	0.0	0.0	-0.004	0.0
$\mathbf{d}_{x^2y^2}$	0.0	-0.003	-0.004	-10.997	-0.092
\mathbf{d}_{xy}	0.028	0.0	0.0	-0.092	-0.008

SUPPLEMENTARY TABLE 39. Orbital resolved exchange parameters for the spin polarized optimized structure of NiPS₃.

\mathbf{J}_1 (meV)	\mathbf{d}_{z^2}	\mathbf{d}_{xz}	\mathbf{d}_{yz}	$\mathbf{d}_{x^2y^2}$	\mathbf{d}_{xy}
\mathbf{d}_{z^2}	0.099	0.009	0.007	-0.05	0.007
\mathbf{d}_{xz}	0.009	0.004	-0.002	0.044	-0.0
\mathbf{d}_{yz}	0.007	-0.002	0.002	0.038	-0.0
$\mathbf{d}_{x^2y^2}$	-0.05	0.044	0.038	-0.219	-0.003
\mathbf{d}_{xy}	0.007	-0.0	-0.0	-0.003	-0.004

SUPPLEMENTARY TABLE 40. Orbital resolved exchange parameters for the spin polarized optimized structure of NiPS₃.

\mathbf{J}_2 (meV)	\mathbf{d}_{z^2}	\mathbf{d}_{xz}	\mathbf{d}_{yz}	$\mathbf{d}_{x^2y^2}$	\mathbf{d}_{xy}
\mathbf{d}_{z^2}	-0.17	-0.009	-0.007	0.001	0.08
\mathbf{d}_{xz}	-0.009	-0.008	-0.002	0.007	0.005
\mathbf{d}_{yz}	-0.007	-0.002	-0.009	0.007	0.004
$\mathbf{d}_{x^2y^2}$	0.001	0.007	0.007	0.054	-0.004
\mathbf{d}_{xy}	0.08	0.005	0.004	-0.004	0.002

SUPPLEMENTARY TABLE 41. Orbital resolved exchange parameters for the spin polarized optimized structure of NiPS₃.

\mathbf{J}_3 (meV)	\mathbf{d}_{z^2}	\mathbf{d}_{xz}	\mathbf{d}_{yz}	$\mathbf{d}_{x^2y^2}$	\mathbf{d}_{xy}
\mathbf{d}_{z^2}	0.012	-0.002	-0.001	-0.013	0.001
\mathbf{d}_{xz}	-0.002	-0.001	-0.001	0.008	-0.0
\mathbf{d}_{yz}	-0.001	-0.001	-0.0	0.008	-0.001
$\mathbf{d}_{x^2y^2}$	-0.013	0.008	0.008	0.028	0.01
\mathbf{d}_{xy}	0.001	-0.0	-0.001	0.01	-0.001

SUPPLEMENTARY TABLE 42. Orbital resolved exchange parameters for the spin polarized optimized structure of NiPS₃.

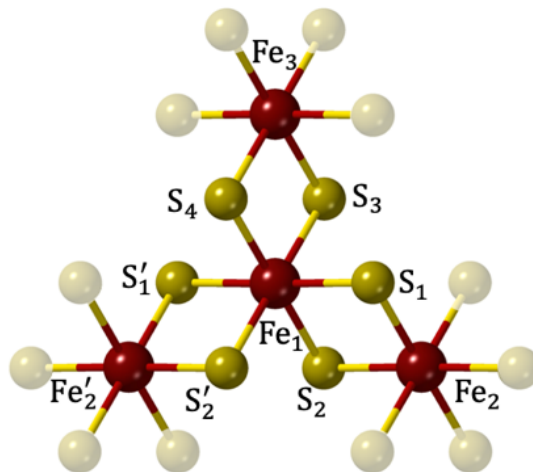
\mathbf{J}_4 (meV)	\mathbf{d}_{z2}	\mathbf{d}_{xz}	\mathbf{d}_{yz}	\mathbf{d}_{x2y2}	\mathbf{d}_{xy}
\mathbf{d}_{z2}	0.116	0.002	0.002	0.028	-0.006
\mathbf{d}_{xz}	0.002	-0.002	0.0	0.0	0.0
\mathbf{d}_{yz}	0.002	0.0	-0.002	0.0	0.0
\mathbf{d}_{x2y2}	0.028	0.0	0.0	-0.028	-0.01
\mathbf{d}_{xy}	-0.006	0.0	0.0	-0.01	0.0

SUPPLEMENTARY TABLE 43. Orbital resolved exchange parameters for the spin polarized optimized structure of NiPS₃.

\mathbf{J}_5 (meV)	\mathbf{d}_{z2}	\mathbf{d}_{xz}	\mathbf{d}_{yz}	\mathbf{d}_{x2y2}	\mathbf{d}_{xy}
\mathbf{d}_{z2}	-4.91	-0.056	-0.046	-2.12	-0.032
\mathbf{d}_{xz}	-0.056	-0.009	0.0	-0.013	0.0
\mathbf{d}_{yz}	-0.046	0.0	-0.008	-0.007	-0.0
\mathbf{d}_{x2y2}	-2.12	-0.013	-0.007	-0.353	-0.003
\mathbf{d}_{xy}	-0.032	0.0	-0.0	-0.003	-0.001

SUPPLEMENTARY TABLE 44. Orbital resolved exchange parameters for the spin polarized optimized structure of NiPS₃.

\mathbf{J}_6 (meV)	\mathbf{d}_{z2}	\mathbf{d}_{xz}	\mathbf{d}_{yz}	\mathbf{d}_{x2y2}	\mathbf{d}_{xy}
\mathbf{d}_{z2}	-0.04	-0.002	-0.002	0.0	0.048
\mathbf{d}_{xz}	-0.002	0.0	0.0	-0.003	0.0
\mathbf{d}_{yz}	-0.002	0.0	0.0	-0.004	0.0
\mathbf{d}_{x2y2}	0.0	-0.003	-0.004	-10.334	-0.07
\mathbf{d}_{xy}	0.048	0.0	0.0	-0.07	-0.012

SUPPLEMENTARY FIG. 8. Top view of a cluster of single-layer FePS₃ centered in Fe₁ labelling the first Fe atoms neighbours and the S atoms that mediate super-exchange magnetic interactions.

SUPPLEMENTARY TABLE 45. Hopping parameters for the crystallographic structure of FePS₃.

		$\mathbf{S}_1(\mathbf{p}_z)$	$\mathbf{S}_1(\mathbf{p}_x)$	$\mathbf{S}_1(\mathbf{p}_y)$	$\mathbf{S}_2(\mathbf{p}_z)$	$\mathbf{S}_2(\mathbf{p}_x)$	$\mathbf{S}_2(\mathbf{p}_y)$
Fe₁	\mathbf{d}_{z2}	1.089	-0.079	-0.243	0.054	-0.012	-0.608
	\mathbf{d}_{xz}	-0.124	-0.331	-0.029	-0.041	-0.021	0.028
	\mathbf{d}_{yz}	-0.254	-0.100	-0.357	-0.427	0.127	-0.002
	\mathbf{d}_{x2y2}	0.002	-0.005	-0.037	0.127	-0.086	-0.987
	\mathbf{d}_{xy}	0.003	0.021	0.038	0.037	-0.341	0.181
Fe₂	\mathbf{d}_{z2}	-0.054	0.012	0.608	-1.089	0.079	0.243
	\mathbf{d}_{xz}	0.041	0.021	-0.028	0.124	0.331	0.029
	\mathbf{d}_{yz}	0.427	-0.127	0.002	0.254	0.100	0.357
	\mathbf{d}_{x2y2}	-0.127	0.086	0.987	-0.002	0.005	0.037
	\mathbf{d}_{xy}	-0.037	0.341	-0.181	-0.003	-0.021	-0.038

SUPPLEMENTARY TABLE 46. Hopping parameters for the crystallographic structure of FePS₃.

		$\mathbf{S}_3(\mathbf{p}_z)$	$\mathbf{S}_3(\mathbf{p}_x)$	$\mathbf{S}_3(\mathbf{p}_y)$	$\mathbf{S}_4(\mathbf{p}_z)$	$\mathbf{S}_4(\mathbf{p}_x)$	$\mathbf{S}_4(\mathbf{p}_y)$
Fe₁	\mathbf{d}_{z2}	0.015	-0.525	-0.037	-0.015	0.040	0.525
	\mathbf{d}_{xz}	-0.274	-0.023	-0.031	-0.020	-0.008	-0.029
	\mathbf{d}_{yz}	0.037	0.030	0.010	0.276	0.030	0.026
	\mathbf{d}_{x2y2}	-0.036	0.942	0.032	-0.028	0.078	0.939
	\mathbf{d}_{xy}	-0.070	-0.043	-0.325	0.075	0.319	-0.078
Fe₃	\mathbf{d}_{z2}	0.023	-0.056	-0.562	-0.022	0.562	0.053
	\mathbf{d}_{xz}	0.028	0.018	0.062	0.334	-0.016	0.012
	\mathbf{d}_{yz}	-0.336	-0.011	0.011	-0.049	-0.062	-0.018
	\mathbf{d}_{x2y2}	0.041	-0.117	-1.048	0.052	-1.050	-0.058
	\mathbf{d}_{xy}	-0.096	-0.414	0.080	0.090	0.056	0.423

SUPPLEMENTARY TABLE 47. Hopping parameters for the crystallographic structure of CoPS₃.

		$\mathbf{S}_1(\mathbf{p}_z)$	$\mathbf{S}_1(\mathbf{p}_x)$	$\mathbf{S}_1(\mathbf{p}_y)$	$\mathbf{S}_2(\mathbf{p}_z)$	$\mathbf{S}_2(\mathbf{p}_x)$	$\mathbf{S}_2(\mathbf{p}_y)$
Co₁	\mathbf{d}_{z2}	1.019	-0.281	-0.178	0.032	-0.174	-0.581
	\mathbf{d}_{xz}	-0.229	-0.339	0.098	-0.069	-0.032	0.039
	\mathbf{d}_{yz}	-0.284	0.040	-0.341	-0.431	0.024	-0.056
	\mathbf{d}_{x2y2}	-0.003	0.003	-0.043	0.059	-0.405	-0.902
	\mathbf{d}_{xy}	-0.001	0.017	0.036	-0.089	-0.35	0.381
Co₂	\mathbf{d}_{z2}	-0.032	0.174	0.581	-1.019	0.279	0.178
	\mathbf{d}_{xz}	0.069	0.032	-0.039	0.229	0.339	-0.097
	\mathbf{d}_{yz}	0.431	-0.025	0.056	0.284	-0.041	0.341
	\mathbf{d}_{x2y2}	-0.059	0.406	0.901	0.003	-0.003	0.043
	\mathbf{d}_{xy}	0.089	0.350	-0.382	0.001	-0.017	-0.036

SUPPLEMENTARY TABLE 48. Hopping parameters for the crystallographic structure of CoPS₃.

		$\mathbf{S}_3(\mathbf{p}_z)$	$\mathbf{S}_3(\mathbf{p}_x)$	$\mathbf{S}_3(\mathbf{p}_y)$	$\mathbf{S}_4(\mathbf{p}_z)$	$\mathbf{S}_4(\mathbf{p}_x)$	$\mathbf{S}_4(\mathbf{p}_y)$
Co₁	\mathbf{d}_{z2}	0.017	-0.489	-0.033	-0.018	0.035	0.488
	\mathbf{d}_{xz}	-0.241	-0.043	-0.014	-0.029	-0.013	-0.034
	\mathbf{d}_{yz}	0.044	0.037	0.014	0.243	0.014	0.046
	\mathbf{d}_{x2y2}	-0.042	0.904	0.011	-0.034	0.051	0.908
	\mathbf{d}_{xy}	-0.072	-0.094	-0.299	0.077	0.296	-0.019
Co₃	\mathbf{d}_{z2}	0.015	-0.031	-0.534	-0.015	0.534	0.029
	\mathbf{d}_{xz}	0.037	0.020	0.056	0.282	0.011	0.015
	\mathbf{d}_{yz}	-0.285	-0.015	-0.015	-0.054	-0.057	-0.020
	\mathbf{d}_{x2y2}	0.037	-0.036	-1.011	0.046	-1.005	0.009
	\mathbf{d}_{xy}	-0.089	-0.341	0.012	0.083	0.113	0.341

SUPPLEMENTARY TABLE 49. Hopping parameters for the crystallographic structure of NiPS₃.

		$\mathbf{S}_1(\mathbf{p}_z)$	$\mathbf{S}_1(\mathbf{p}_x)$	$\mathbf{S}_1(\mathbf{p}_y)$	$\mathbf{S}_2(\mathbf{p}_z)$	$\mathbf{S}_2(\mathbf{p}_x)$	$\mathbf{S}_2(\mathbf{p}_y)$
Ni₁	\mathbf{d}_{z2}	1.023	-0.279	-0.112	0.009	-0.116	-0.553
	\mathbf{d}_{xz}	-0.288	-0.316	0.066	-0.055	-0.038	0.047
	\mathbf{d}_{yz}	-0.166	0.053	-0.352	-0.367	-0.011	0.015
	\mathbf{d}_{x2y2}	0.032	0.025	-0.022	0.044	-0.237	-0.890
	\mathbf{d}_{xy}	-0.017	-0.008	0.053	-0.057	-0.320	0.262
Ni₂	\mathbf{d}_{z2}	-0.008	0.118	0.553	-1.026	0.275	0.113
	\mathbf{d}_{xz}	0.055	0.038	-0.047	0.288	0.316	-0.065
	\mathbf{d}_{yz}	0.366	0.009	-0.015	0.166	-0.055	0.353
	\mathbf{d}_{x2y2}	-0.043	0.241	0.889	-0.032	-0.025	0.022
	\mathbf{d}_{xy}	0.058	0.320	-0.263	0.017	0.008	-0.053

SUPPLEMENTARY TABLE 50. Hopping parameters for the crystallographic structure of NiPS₃.

		$\mathbf{S}_3(\mathbf{p}_z)$	$\mathbf{S}_3(\mathbf{p}_x)$	$\mathbf{S}_3(\mathbf{p}_y)$	$\mathbf{S}_4(\mathbf{p}_z)$	$\mathbf{S}_4(\mathbf{p}_x)$	$\mathbf{S}_4(\mathbf{p}_y)$
Ni₁	\mathbf{d}_{z2}	0.034	-0.526	-0.061	-0.035	0.064	0.525
	\mathbf{d}_{xz}	-0.331	-0.053	-0.030	-0.011	-0.016	-0.031
	\mathbf{d}_{yz}	0.039	0.036	0.019	0.333	0.030	0.057
	\mathbf{d}_{x2y2}	-0.069	0.971	0.090	-0.057	0.160	0.955
	\mathbf{d}_{xy}	-0.068	0.003	-0.389	0.080	0.369	-0.170
Ni₃	\mathbf{d}_{z2}	0.032	-0.05	-0.556	-0.031	0.557	0.047
	\mathbf{d}_{xz}	0.015	0.017	0.042	0.352	0.032	0.043
	\mathbf{d}_{yz}	-0.355	-0.042	-0.036	-0.045	-0.045	-0.020
	\mathbf{d}_{x2y2}	0.051	-0.140	-1.025	0.062	-1.036	-0.067
	\mathbf{d}_{xy}	-0.082	-0.393	0.159	0.071	0.019	0.408

Supplementary Note 2. LANDAU THEORY OF SECOND-ORDER PHASE TRANSITIONS AND SPONTANEOUS MAGNETOSTRICTION

Magnetostriction is a coupling between magnetic and mechanical parts of our system. This coupling can be described by an energy term in the total free energy of our system [1]. We can then write the total free energy as

$$F - F_0 = U_{\text{el}}(z) + a(T - T_N)^{2\beta} L_i L_i + B L_i L_i L_i L_i - \sigma_{ij}(z) \lambda_{ijkl} L_k L_l. \quad (7)$$

Here F is the total free energy of in the AF phase at zero magnetic field, F_0 is the free energy of paramagnetic phase, $U_{\text{el}}(z)$ is the elastic energy of a membrane with deflection z at its centre, T is the temperature of our system and T_N is the Néel temperature, L_i are the components of the Néel vector, β is a critical exponent, a and B are positive constants, $\sigma_{ij}(z)$ is the stress tensor and λ_{ijkl} is the magnetostriction tensor. The last term couples the stress to the Néel vector thereby describing the magnetostriction. If we assume the Néel vector to be fully aligned with the easy axis, Eq. (7) simplifies to:

$$F - F_0 = U_{\text{el}}(z) + a(T - T_N)^{2\beta} L^2 + B L^4 - \sigma_{ij}(z) \lambda_{ij} L^2, \quad (8)$$

where L is the magnetic order parameter (i.e. the magnitude of the Néel vector). For notational convenience we write λ_{ij} in dropping the third and fourth index of λ_{ijkl} as only the component where kl corresponds to the easy axis contributes. The elastic energy in a homogeneous membrane is given by [2]

$$U_{\text{el}} = \int \int \frac{S_{ijkl}}{2} \sigma_{ij}(x, y, z) \sigma_{kl}(x, y, z) dx dy, \quad (9)$$

where the integration runs over the in plane dimensions of the membrane, z is the membrane deflection at its centre and should not be confused with the out of plane coordinate. For ease of notation we will not explicitly write the integration and coordinate dependence from here on. Assuming the membrane thickness does not vary significantly we can take the out of plane component stress component to vanish, $\sigma_{zx} = \sigma_{zy} = \sigma_{zz} = 0$. Eq. (9) then simplifies to

$$U_{\text{el}} = \frac{S_{xxxx}}{2} \sigma_{xx} \sigma_{xx} + \frac{S_{yyyy}}{2} \sigma_{yy} \sigma_{yy} + S_{xxyy} \sigma_{xx} \sigma_{yy} + S_{xxxy} \sigma_{xx} \sigma_{xy} + S_{yyxy} \sigma_{yy} \sigma_{xy} + \frac{S_{xyxy}}{2} \sigma_{xy} \sigma_{xy}. \quad (10)$$

Taking our coordinates such that x, y correspond with the principle stress directions all terms containing σ_{xy} vanish. This simplifies the elastic energy further to

$$U_{\text{el}} = \frac{S_{xxxx}}{2} \sigma_{xx} \sigma_{xx} + \frac{S_{yyyy}}{2} \sigma_{yy} \sigma_{yy} + S_{xxyy} \sigma_{xx} \sigma_{yy}. \quad (11)$$

Assuming the material has isotropic elastic properties the relevant compliance tensor components are

$$S_{xxxx} = S_{yyyy} = \frac{1}{E} \text{ and } S_{xxyy} = \frac{-\nu}{E}. \quad (12)$$

Substituting this in to Eq. (11) we find

$$U_{\text{el}} = \frac{1}{2E} \sigma_{xx} \sigma_{xx} + \frac{1}{2E} \sigma_{yy} \sigma_{yy} - \frac{\nu}{E} \sigma_{xx} \sigma_{yy}. \quad (13)$$

By taking the derivative of the free energy with respect to either z or L we find the forces acting on these degrees of freedom, ϕ_L and ϕ_z respectively to be given by

$$-\phi_L = \frac{d(F - F_0)}{dL} = 2a(T - T_N)^{2\beta} L + 4BL^3 - 2\sigma_{ij}(z) \lambda_{ij} L, \quad (14)$$

$$-\phi_z = \frac{d(F - F_0)}{dz} = (S_{ijkl} \sigma_{ij}(z) + \lambda_{kl} L^2) \frac{d\sigma_{kl}(z)}{dz}. \quad (15)$$

Order parameter and critical exponent

In order to find an equation that describes the order parameter as a function of temperature, we find a solution for equation (14) for the case where $\phi_L = 0$. Aside from the trivial solution $L = 0$, we find for below the transition the additional solution:

$$L^2 = -\frac{a}{2B} (T - T_N)^{2\beta} + \frac{\sigma_{ij} \lambda_{ij}}{2B}, \quad (16)$$

which could be rewritten for $T_N^* = T_N - \left(\frac{\sigma_{ij}\lambda_{ij}}{a}\right)^{\frac{1}{2\beta}}$ [3] as:

$$L^2 = \frac{a}{2B}(T_N^* - T)^{2\beta}. \quad (17)$$

This equation now describes the temperature dependence of the order parameter in a critical region near T_N with a corresponding critical exponent β .

Magnetostrictive strain and resonance frequency

To assess the magnetostriction contribution to strain and thus the frequency of a rectangular membrane resonator, we need to find stiffness of the membrane from its force-deflection equation. In doing that we analyse equation (15). First, we describe strain equation for the rectangular membrane at its centre as:

$$\epsilon_{xx}(z) = \epsilon_{0,x} + \frac{c_1}{2} \frac{z^2}{l^2} \quad (18a)$$

$$\epsilon_{yy}(z) = \epsilon_{0,y} + \frac{c_1}{2} \frac{z^2}{w^2} \quad (18b)$$

where c_1 is a geometrical pre-factor that describes the deflection shape of the fundamental mode of vibration [4, 5]. For $w \ll l$ we can neglect the z dependence of $\epsilon_{xx}(z)$. Now, we substitute (18) to (15), using the relation $\sigma_{ij} = C_{ijkl}\epsilon_{kl}$, we find

$$-\phi_z = \left(\frac{E}{1-\nu^2}\epsilon_{0,y} + \frac{\nu E}{1-\nu^2}\epsilon_{0,x} - \lambda_{yy}L^2 \right) \frac{c_1}{w^2}z + \frac{E}{1-\nu^2} \frac{c_1^2}{2} \frac{z^3}{w^4}, \quad (19)$$

where we used that $C_{xxxx} = C_{yyyy} = \frac{E}{1-\nu^2}$ and $C_{yyxx} = C_{xxyy} = \frac{\nu E}{1-\nu^2}$. Eq. (19) becomes

$$-\phi_z = k_1 z - \frac{\lambda_{ij}c_1}{w^2}L^2 z + k_3 z^3 \quad (20)$$

where k_1 is the elastic linear stiffness and k_3 is the cubic elastic stiffness, given by

$$k_1 = \frac{E}{1-\nu^2}(\epsilon_{0,y} + \nu\epsilon_{0,x}) \frac{c_1}{w^2} \quad (21)$$

$$k_3 = \frac{E}{1-\nu^2} \frac{c_1^2}{2w^4}. \quad (22)$$

Assuming small deflections we can neglect the z^3 contribution in eq. (19) and find that the linear stiffness is changed with respect to the purely elastic case. If we consider a rectangular cavity with its long axis is parallel to the crystalline axis b or a respectively we find:

$$-\phi_{z \text{ b,a}} = \left(k_1 - \frac{c_1}{w^2}\lambda_{a,b}L^2 \right) z, \quad (23)$$

where $\lambda_{a,b}$ are the phenomenological magnetostriction coefficients, chosen such that to couple a and b crystalline directions and L . That leads to a change in the effective linear stiffness $k_{b,a}$:

$$k_{b,a} = k_1 - \frac{c_1}{w^2}\lambda_{a,b}L^2, \quad (24)$$

which can be used to write down the frequency equations using $f_{a,b} = \frac{1}{2\pi}\sqrt{\frac{k_{a,b}}{m}}$,

$$f_b \approx \frac{1}{2\pi} \sqrt{\frac{1}{m} \frac{c_1}{w^2} \left[\frac{E}{1-\nu^2}(\epsilon_{0,a} + \nu\epsilon_{0,b}) - \lambda_a L^2 \right]}, \quad (25a)$$

$$f_a \approx \frac{1}{2\pi} \sqrt{\frac{1}{m} \frac{c_1}{w^2} \left[\frac{E}{1-\nu^2}(\epsilon_{0,b} + \nu\epsilon_{0,a}) - \lambda_b L^2 \right]}, \quad (25b)$$

where m is the mass of the membrane. And define magnetostrictive strain by:

$$\epsilon_{ms,a} = \frac{c_1}{mw^2} \lambda_a L^2, \quad (26)$$

$$\epsilon_{ms,b} = \frac{c_1}{mw^2} \lambda_b L^2. \quad (27)$$

Taking a difference of the squares of equations (25) and assuming $\epsilon_{0,a} = \epsilon_{0,b}$, we arrive at the final equation:

$$f_b^2 - f_a^2 = -\frac{1}{4\pi^2} \frac{c_1}{mw^2} [\lambda_b - \lambda_a] L^2, \quad (28)$$

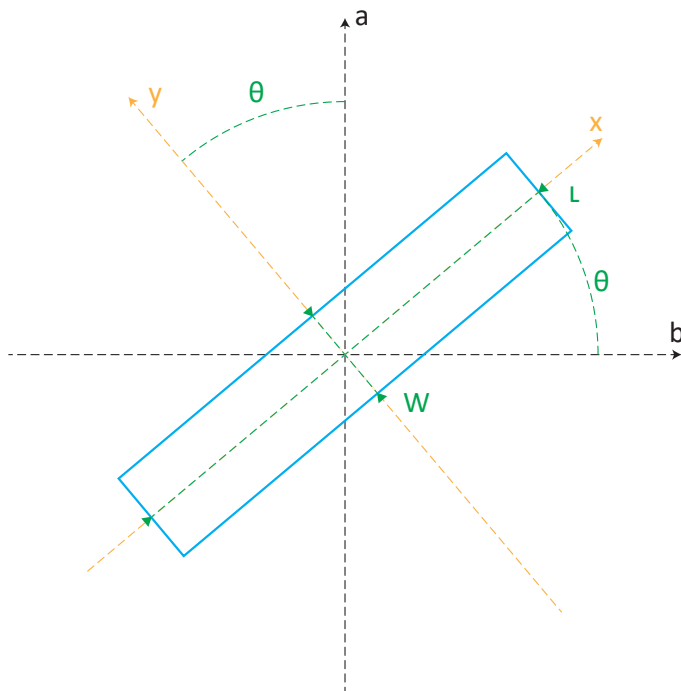
which relates antiferromagnetic order parameter L and measured resonance frequencies of orthogonal resonators aligned to crystalline axes $f_{a,b}$ in ordered phase. Finally, one can show that by plugging equation (17) to (28):

$$f_b^2 - f_a^2 \propto (T_N^* - T)^{2\beta}, \quad (29)$$

which could be used to fit experimental data to extract critical exponent β near the phase transition temperature T_N^* .

Supplementary Note 3. DERIVATION OF ANISOTROPIC RESONANCE FREQUENCY

Here, we derive the general equation of the resonance frequency of a rectangular cavity oriented at an angle θ with respect to the crystalline axes, as schematically shown in Fig. 9. The global coordinate system is defined by the crystallographic axes a and b , along which the material deforms resulting in stresses σ_{aa} and σ_{bb} . The longest side of the cavity, with length l , can be oriented at an arbitrary angle θ with respect to b .



SUPPLEMENTARY FIG. 9. **Schematic illustration of rectangular membrane** Rectangular membrane of width w and length l oriented with its long side at an angle θ with respect to the crystalline direction b . The x - y direction refer to the main directions of the rectangular membrane.

Let us first consider a cavity oriented parallel to a crystallographic axis. Since the membranes are very thin, we can assume that the stress in the direction perpendicular to the plane is zero, $\sigma_{cc} = 0$, the membrane's stress tensor can be expressed as

$$\boldsymbol{\sigma} = \begin{pmatrix} \sigma_{aa} & \sigma_{ab} \\ \sigma_{ba} & \sigma_{bb} \end{pmatrix}_{ab}, \quad (30)$$

where the subscript $(\)_{ab}$ indicates we expressed the stress tensor in the basis of the crystallographic coordinate system. If we assume that there are no shear forces acting on the crystal lattice, $\sigma_{ab} = \sigma_{ba} = 0$, there will be no shear on cavities oriented along the main crystallographic axes. Now, if we consider a rectangular cavity rotated by θ with respect to the crystallographic axes, we can define a rotated xy -coordinate system oriented along the main axis of the rectangle. To express $\boldsymbol{\sigma}$ in this coordinate system we use the tensor transformation rule, $\sigma'_{ij} = q_{ki}q_{lj}\sigma_{kl}$ where q_{ij} are components of the rotation tensor transforming the ab -coordinate system, \mathbf{e} , into the xy -coordinate system, \mathbf{e}' as $\mathbf{e}'_i = q_{ij}\mathbf{e}_j$. We then get:

$$\boldsymbol{\sigma} = \begin{pmatrix} \sigma_{xx} & \sigma_{xy} \\ \sigma_{yx} & \sigma_{yy} \end{pmatrix}_{xy} = \begin{pmatrix} \cos^2(\theta)\sigma_{aa} + \sin^2(\theta)\sigma_{bb} & -\cos(\theta)\sin(\theta)\sigma_{aa} + \sin(\theta)\cos(\theta)\sigma_{bb} \\ -\sin(\theta)\cos(\theta)\sigma_{aa} + \sin(\theta)\cos(\theta)\sigma_{bb} & \sin^2(\theta)\sigma_{aa} + \cos^2(\theta)\sigma_{bb} \end{pmatrix}_{xy}, \quad (31)$$

Then, the resonance frequency of a rectangular membrane oriented at an angle θ with respect to the crystallographic axis can be expressed as

$$f_\theta \approx \frac{1}{2} \sqrt{\frac{1}{\rho} \left(\frac{\sigma_{xx}}{l^2} + \frac{\sigma_{yy}}{w^2} \right)}. \quad (32)$$

In the case of high-aspect ratio membranes ($w \ll l$), Eq. 32 can be approximated to

$$f_\theta \approx \frac{1}{2} \sqrt{\frac{1}{\rho} \frac{\sigma_{yy}}{w^2}} = \frac{1}{2} \sqrt{\frac{1}{\rho w^2} (\sin^2(\theta)\sigma_{aa} + \cos^2(\theta)\sigma_{bb})}, \quad (33)$$

which is Eq. 3 of the main text.

Now, let us consider the constitutive equations of the material:

$$c_1 = E(\epsilon_{\text{fab},aa} - \epsilon_{\text{th},aa} - \epsilon_{\text{ms},aa}) = E \left(\epsilon_{\text{fab},aa} - \int_{T_0}^{T_1} \alpha_a(T) dT - \lambda_a L^2(T_1) \right) = \sigma_{aa}(T_1) - \nu \sigma_{bb}(T_1) \quad (34)$$

$$c_2 = E(\epsilon_{\text{fab},bb} - \epsilon_{\text{th},bb} - \epsilon_{\text{ms},bb}) = E \left(\epsilon_{\text{fab},bb} - \int_{T_0}^{T_1} \alpha_b(T) dT - \lambda_b L^2(T_1) \right) = \sigma_{bb}(T_1) - \nu \sigma_{aa}(T_1), \quad (35)$$

where ϵ_{fab} is residual fabrication strain at $T = T_0$, ϵ_{th} and ϵ_{ms} are respectively the thermal expansion and magnetostriction contributions to strain, α is the thermal expansion coefficient, λ the magnetostriction coefficient and E is the Young's modulus, which is assumed to be isotropic. We can thus write

$$\sigma_{aa} = c_1 + \nu \sigma_{bb} \quad (36)$$

$$\sigma_{bb} = c_2 + \nu \sigma_{aa}, \quad (37)$$

which can be combined in the following expressions for σ_{aa} and σ_{bb} :

$$\sigma_{aa} = \frac{c_1 + \nu c_2}{1 - \nu^2} \quad (38)$$

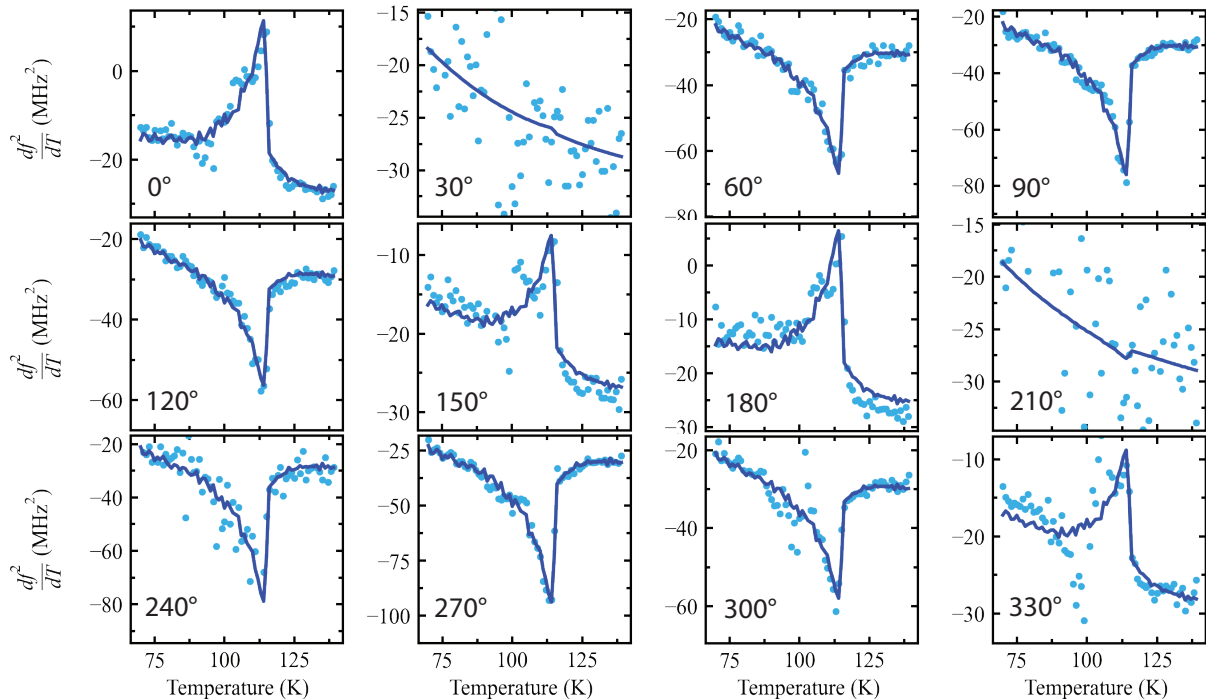
$$\sigma_{bb} = \frac{c_2 + \nu c_1}{1 - \nu^2}. \quad (39)$$

We can now rewrite Eq. 33 in terms of the different contributions to strain, i.e. residual strain from fabrication (ϵ_{fab}), thermal expansion ($\propto \alpha$) and magnetostriction ($\propto \lambda$):

$$f_\theta(T) = \frac{1}{2} \sqrt{\frac{E}{\rho w^2 (1 - \nu^2)} [\sin^2 \theta (c_1 + \nu c_2) + \cos^2 \theta (c_2 + \nu c_1)]} \quad (40)$$

$$= \frac{1}{2} \sqrt{\frac{E}{\rho w^2 (1 - \nu^2)} [(\sin^2 \theta + \nu \cos^2 \theta)(\epsilon_{\text{fab},aa} - \epsilon_{\text{th},aa} - \epsilon_{\text{ms},aa}) + (\cos^2 \theta + \nu \sin^2 \theta)(\epsilon_{\text{fab},bb} - \epsilon_{\text{th},bb} - \epsilon_{\text{ms},bb})]}. \quad (41)$$

Which is consistent with Eq. (25). We can eliminate the pretension ϵ_{fab} terms by considering $\tilde{f}_\theta(T) = f_\theta(T) - f_\theta(T_0)$. In the following, we assume that the only anisotropic temperature-dependent contribution to the total strain comes



SUPPLEMENTARY FIG. 10. **Angle-resolved** $\frac{df^2}{dT}$: Plot of measured (light blue dots) $\frac{df^2}{dT}$ and fit to $b_1 C_{\text{Debye}} + b_2 \frac{dL^2}{dT}$ (blue full line) for all angles of a star-shaped array of CoPS₃.

from magnetostriction, thus we take $\epsilon_{\text{th},aa} = \epsilon_{\text{th},bb} = \epsilon_{\text{th}}$. By definition of θ we have $b \rightarrow \theta = 0^\circ$ and $a \rightarrow \theta = 90^\circ$. From Eq. (41), we then find that $\tilde{f}_a^2 - \tilde{f}_b^2$ becomes

$$\tilde{f}_a^2 - \tilde{f}_b^2 = \frac{E}{4\rho w^2(1+\nu)} (-\epsilon_{\text{ms},aa} + \epsilon_{\text{ms},bb}) \quad (42)$$

$$= -\frac{E}{4\rho w^2(1+\nu)} (\lambda_a - \lambda_b) L^2 \quad (43)$$

from which we can directly extract the order parameter. The thermal expansion contribution to strain ϵ_α is proportional to the integral over the temperature of the thermal expansion coefficient α , which is proportional to the Debye specific heat, C_{Debye} , via the Grünesen parameter. Thus, the derivative with respect to temperature of f_θ^2

$$\frac{df_\theta^2}{dT} = \frac{E}{4\rho w^2(1-\nu^2)} \left[(\sin^2 \theta + \nu \cos^2 \theta) \left(-\alpha - \lambda_a \frac{dL^2}{dT} \right) + (\cos^2 \theta + \nu \sin^2 \theta) \left(-\alpha - \lambda_b \frac{dL^2}{dT} \right) \right] \quad (44)$$

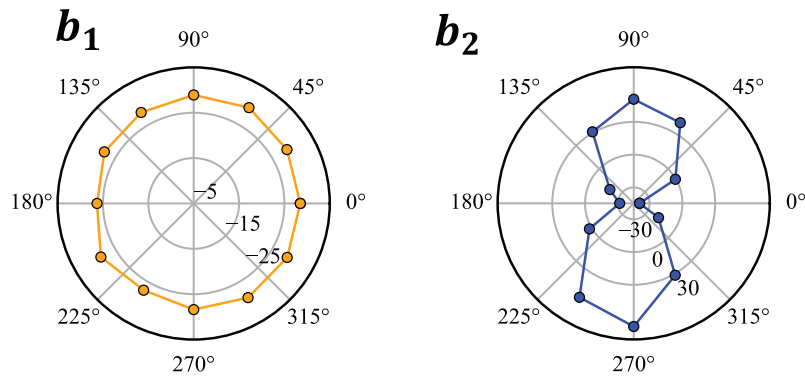
$$= \frac{-E}{4\rho w^2(1-\nu^2)} \left[\alpha(1+\nu) + \left(\sin^2 \theta (\lambda_a + \nu \lambda_b) \frac{dL^2}{dT} + \cos^2 \theta (\lambda_b + \nu \lambda_a) \frac{dL^2}{dT} \right) \right]. \quad (45)$$

can be fitted to $b_1 C_{\text{Debye}} + b_2 \frac{dL^2}{dT}$ where b_1 and b_2 are fit parameters, and $\frac{dL^2}{dT}$ is estimated from Eq. 43. The results of these fits along to measured data of $\frac{df_\theta^2}{dT}$ are shown in Fig. 10. Polar plot of the resulting $b_1(\theta)$ and $b_2(\theta)$ are shown in Fig. 11, which confirm that the thermal contribution to strain does not exhibit significant anisotropic behavior. From Eq. 42 and 40, the expected angle dependance of the parameter b_2 is

$$b_2(\theta) = \left(\frac{E}{4\rho w^2(1-\nu^2)} \right)^2 (1-\nu)(\lambda_a - \lambda_b) [(\sin^2 \theta (\lambda_a + \nu \lambda_b) + \cos^2 \theta (\lambda_b + \nu \lambda_a))], \quad (46)$$

which we use to fit $b_2(\theta)$ in Fig.11 to $A \sin^2 \theta + B \cos^2 \theta$ where

$$\frac{A}{B} = \frac{\lambda_a + \nu \lambda_b}{\lambda_b + \nu \lambda_a}. \quad (47)$$

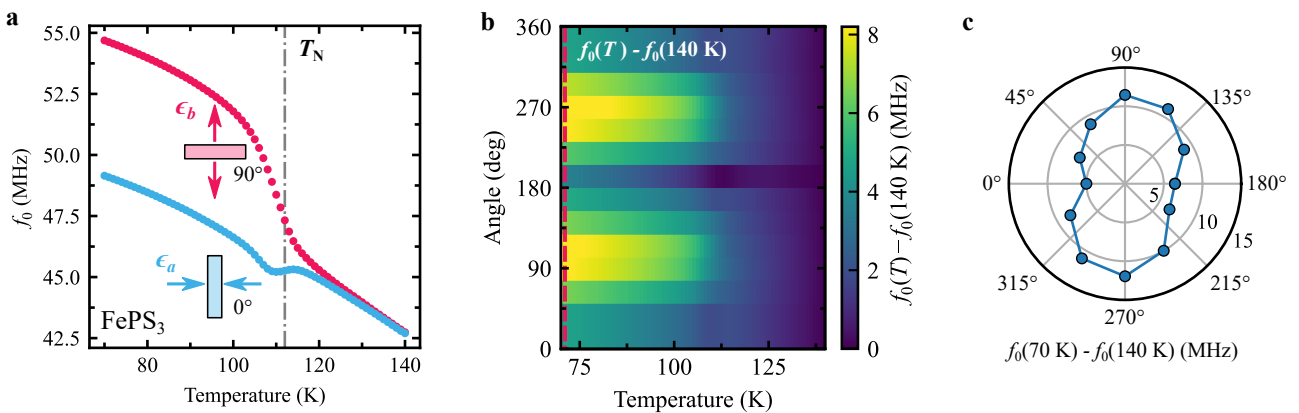


SUPPLEMENTARY FIG. 11. **Polar plot of fit parameters b_1 and b_2** : Polar plot of fit parameters b_1 and b_2 from the fits to df^2/dT shown in Fig. 10.

The fit yields $A/B = -2.062$ and -1.798 for CoPS_3 and $A/B = -5.025$ and -8.695 for FePS_3 .

Supplementary Note 4. ANISOTROPIC RESONANCE FREQUENCY OF FePS_3 RESONATORS

Figure 12 shows resonance frequency data measured on FePS_3 star-cavity resonators, as presented in Fig. 2 of the main text for CoPS_3 and NiPS_3 samples. Figure 12a shows the temperature dependence of the resonance frequency of membranes oriented along the a -axis (in red) and b -axis (in blue). Similarly to CoPS_3 , the opposite strain along a and b arising from spontaneous magnetostriction results in opposite behaviour of the resonance frequency near the transition temperature T_N . The resulting anisotropic response is further illustrated in the map plot of resonance frequency as a function of temperature and angles in Fig. 12b and in the polar plot of $f_{\text{res}}(T) - f_{\text{res}}(140 \text{ K})$ in Fig. 12c.

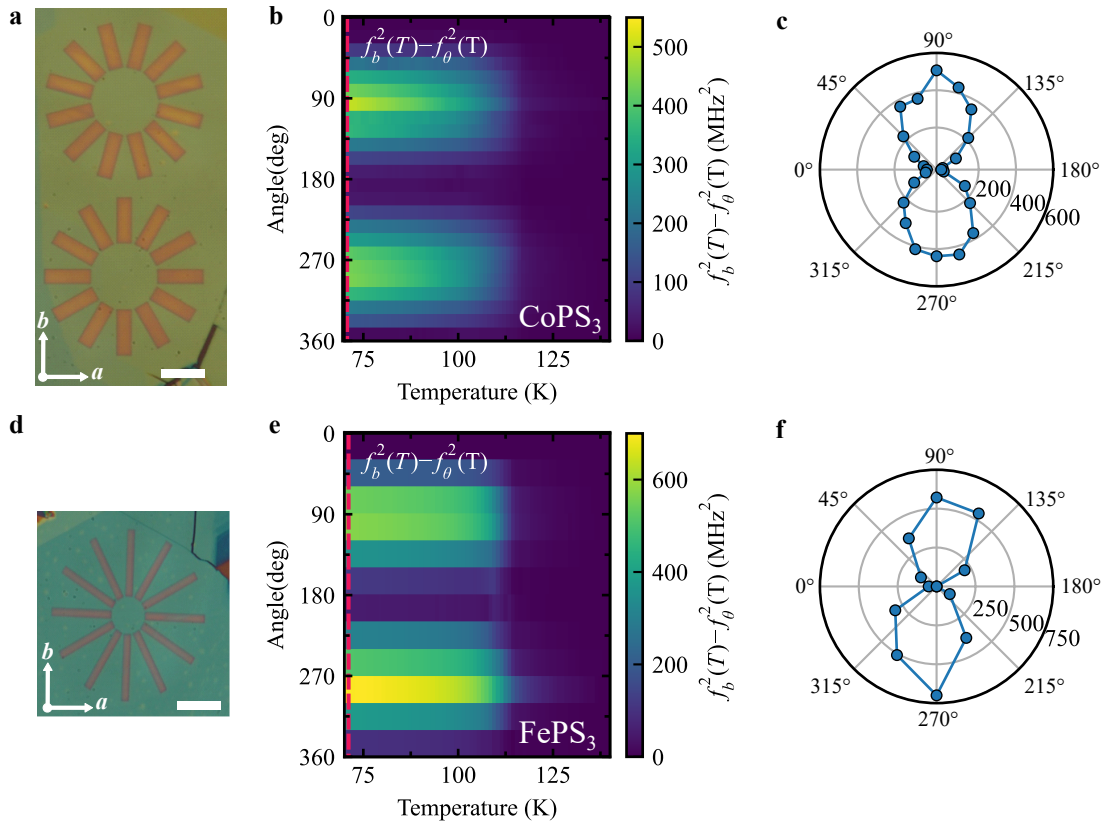


SUPPLEMENTARY FIG. 12. **Angle-resolved resonance frequency data of FePS_3 membranes.** **a** Temperature dependence of f_{res} of a FePS_3 rectangular membrane orientated at 0° (blue) and 90° (red) with respect to the b crystallographic axis. Note that $f_{0,0^\circ}$ and $f_{0,90^\circ}$ are proportional to the strain ϵ_a and ϵ_b respectively (see Eq. 2). The dashed-dotted grey line indicates the transition temperature T_N . **b** Resonance frequency difference, $f_{\text{res}}(T) - f_{\text{res}}(140 \text{ K})$, as a function of angle θ with respect to b -axis and temperature. **c** Polar plot of $f_{\text{res}}(T) - f_{\text{res}}(140 \text{ K})$ taken along the red dashed line in (b).

Supplementary Note 5. ORDER PARAMETER RELATED FREQUENCY DIFFERENCE $\tilde{f}_b^2 - \tilde{f}_\theta^2$

In the main text, we have shown how to relate the difference $f_b^2 - f_a^2$ to the antiferromagnetic order parameter through the magnetostriction induced strain at the phase transition $\epsilon_{\text{ms},aa} = \lambda_a L^2$ and $\epsilon_{\text{ms},bb} = \lambda_b L^2$. In general (see

derivation in Supplementary Note 2), $\tilde{f}_b^2 - \tilde{f}_\theta^2$ is also proportional to L^2 , where \tilde{f}_θ^2 is the pretension corrected resonance frequency of a rectangular cavity oriented at an angle θ with respect to the b -axis. We show this quantity for the CoPS₃ and FePS₃ star-cavity resonators in Fig. 13a,d by plotting $\tilde{f}_b^2 - \tilde{f}_\theta^2$ as a function of angle and temperature in Fig. 13b,e. Figure 13c,f shows the polar plot of $\tilde{f}_b^2 - \tilde{f}_\theta^2$ taken along the red dashed line in 13b,e.



SUPPLEMENTARY FIG. 13. **Angle-resolved data of $f_b^2 - f_\theta^2 \propto L^2$ of CoPS₃ and FePS₃ membranes.** **a,c** Optical image of the CoPS₃ (a) and FePS₃ (c) resonators. Scale bar 12 μm . **b** Resonance frequency difference, $f_b^2 - f_\theta^2 \propto L^2$, as a function of angle θ and temperature of the CoPS₃ sample in (a). **c** Polar plot of $f_b^2 - f_\theta^2$ taken along the red dashed line in (b). **e,f** follows the same structure as (b,c) for the FePS₃ sample in (c).

This behaviour is observed for the thicker samples ($t > 10$ nm) and it is exploited to have a better estimate of the critical parameters β and T_N as discussed in Supplementary Note 6. For thinner resonators every irregularity, like wrinkles or tears, can strongly affect their mode shapes. In some cases, these imperfections can drastically change the resonance frequency of the fundamental mode, as well as its temperature dependence. Therefore, when analysing the critical behaviour of thin flakes, we choose only the most pristine and unaffected membranes out of all fabricated out of a single flake to be sure we are not affected by these irregularities.

Supplementary Note 6. CRITICAL CURVE FIT

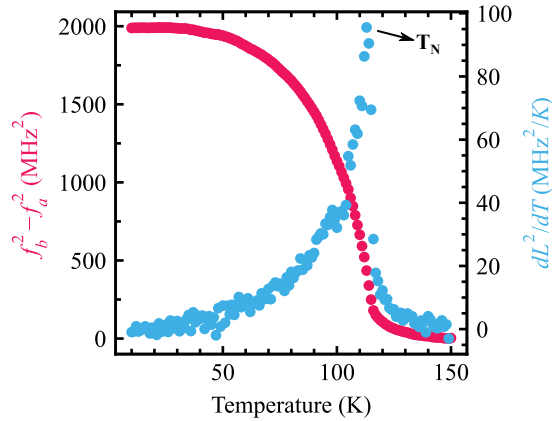
To extract critical parameters β and T_N shown in Fig. 3 and 4 of the main text, we fit the order parameter related difference $f_b^2 - f_a^2 \propto L^2$ to the power law $A_\theta(1 - T/T_N)^{2\beta}$. The experimental determination of critical parameters is often debated due to the difficulty of extracting from one set of data, three strongly correlated parameters, β , T_N and A_θ . In addition, finite size effects are known to smear the transition which usually results in a non-zero tail of the order parameter in the disordered state and makes it harder to unambiguously determine the critical temperature. Also, the choice of the temperature interval for the fit is not universal and it is often arbitrary.

In order to have a better estimate of the critical exponents from our experiments, we compute $f_b^2 - f_\theta^2$ for all θ in a star and fit the data to $A_\theta(1 - T/T_N)^{2\beta}$. For each star, we then calculate the average value and standard deviation of the critical parameters T_N and β weighted by the error from the fit $T_{N,\text{err}}$ and β_{err} .

We start with an initial guess, T_N^* , for T_N by extracting the maximum of the derivative of $f_b^2 - f_\theta^2$ with respect to temperature as shown in Fig. 14. We then fit the $A_\theta(1 - T/T_N)^{2\beta}$ to $f_b^2 - f_\theta^2$ over the range $[\alpha T_N^*, T_N^*]$, for α varying between $[0.85, 0.95]$ allowing A, T_N, β to vary. We then define the total error for each α to be $T_{N,\text{err}} + \beta_{\text{err}}$, where $T_{N,\text{err}}, \beta_{\text{err}}$ are the standard deviation errors of the fit. We then take the extracted T_N, β with corresponding $T_{N,\text{err}}, \beta_{\text{err}}$ to be ones given the fit corresponding to the α minimizing the total error. We repeat this process for each θ yielding a distribution of T_N, β . We then extract a weighted mean of this distribution as follows:

$$\bar{\beta} = \frac{1}{N} \sum_{\theta} \beta \frac{\beta_{\text{err},\text{min}}}{\beta_{\text{err}}} \quad (48)$$

Where N is the number of cavity pairs and $\beta_{\text{err},\text{min}}$ the β_{err} of the pairing with smallest β_{err} . We then fit a normal distribution with $\bar{\beta}$ as mean to the distribution of β where weigh each β by $\frac{\beta_{\text{err},\text{min}}}{\beta_{\text{err}}}$, from which we extract the standard deviation. Repeating this process for T_N . The resulting parameters for each sample are listed in Table 51.



SUPPLEMENTARY FIG. 14. **First estimate of T_N from the derivative of the order parameter.**

Material	Sample	t (nm)	β	T_N (K)
CoPS ₃	1	33	0.28 ± 0.017	115.7 ± 0.38
CoPS ₃	2	52	0.311 ± 0.025	117 ± 0.35
CoPS ₃	3	52	0.298 ± 0.034	116.1 ± 0.18
CoPS ₃	4	8	0.195 ± 0.0446	107.8 ± 2.65
CoPS ₃	5	8.6	0.218 ± 0.002	102.5 ± 1.3
FePS ₃	1	60	0.208 ± 0.0328	112.7 ± 0.87
FePS ₃	2	40	0.203 ± 0.03	109.1 ± 0.37
FePS ₃	3	10	0.194 ± 0.023	110.2 ± 0.48
FePS ₃	4	7	0.206 ± 0.047	107.9 ± 0.76
NiPS ₃	1	48	0.218 ± 0.016	150.7 ± 0.7

SUPPLEMENTARY TABLE 51. **Critical exponents of MPS₃ samples.** Critical exponents, β and T_N , for CoPS₃, FePS₃ and NiPS₃ samples of different thicknesses, extracted following the procedure described in Supplementary Information Supplementary Note 6

-
- [1] Landau, L. D., Pitaevskii, L. P. & Lifshitz, E. M. *Electrodynamics of continuous media*, vol. 8 (Butterworth, New York, 1984), 2 edn.
 - [2] Landau, L. D. & Lifshitz, E. M. *Theory of Elasticity* (Elsevier, 1986), 3 edn.
 - [3] Šiškins, M. *et al.* Magnetic and electronic phase transitions probed by nanomechanical resonators. *Nat. Commun.* **11**, 2698 (2020).
 - [4] Bunch, J. S. *Mechanical and electrical properties of graphene sheets* (Ph.D. thesis, Cornell University Ithaca, NY, 2008).
 - [5] Šiškins, M. *et al.* Highly anisotropic mechanical and optical properties of 2D layered As₂S₃ membranes. *ACS Nano* **13**, 10845–10851 (2019).